

Theory of charge dynamics in bilayer electron system with long-range Coulomb interaction

Hiroyuki Yamase

Research Center of Materials Nanoarchitectonics (MANA),

National Institute for Materials Science (NIMS), Tsukuba 305-0047, Japan

(Dated: November 13, 2024)

Abstract

We perform a comprehensive study of charge excitations in a bilayer electron system in the presence of the long-range Coulomb interaction (LRC). Our major point is to derive formulae of the LRC that fully respect the bilayer lattice structure. This is an extension of the LRC obtained by Fetter in the electron-gas model 50 years ago and can now be applicable to any electron density. We then provide general formulae of the charge susceptibility in the random phase approximation and study them numerically. The charge ordering tendency is not found and instead we find two plasmon modes, ω_+ and ω_- modes. Our second major point is to elucidate their spectral weight distribution and the effect of electron tunneling between the layers. The spectral weight of the ω_{\pm} modes does not have 2π periodicity along the $q_z c$ direction; q_z and c are momentum and the lattice constant along the z direction, respectively. The ω_+ mode loses spectral weight at in-plane momentum $\mathbf{q}_{\parallel} = (0, 0)$ at $q_z c = 2n\pi$ with n being integer whereas the ω_- mode has no spectral weight at $q_z c = 0$ for any \mathbf{q}_{\parallel} but acquires sizable spectral weight at $q_z c = 2n\pi$ with $n \neq 0$. Both ω_{\pm} modes are gapped at $\mathbf{q}_{\parallel} = (0, 0)$. When $q_z c$ is away from $2n\pi$, the ω_{\pm} modes show striking behavior. When the intrabilayer hopping t_z is relatively small (large), the ω_- (ω_+) mode becomes gapless at $\mathbf{q}_{\parallel} = (0, 0)$ whereas the ω_+ (ω_-) mode retains the gap. However, when the interbilayer hopping integral t'_z is taken into account, the gapless mode acquires a gap at $\mathbf{q}_{\parallel} = (0, 0)$ and both ω_{\pm} modes are gapped at any $q_z c$. To highlight the special feature of the LRC, we also clarify a difference to the case of a short-range interaction. While the strong electron correlation effects are not included, the present theory captures available data of the charge excitations observed by resonant inelastic x-ray scattering for Y-based cuprate superconductors.

I. INTRODUCTION

High-temperature cuprate superconductors are realized by carrier doping into antiferromagnetic Mott insulators [1]. The importance of spin fluctuations was widely recognized for the high- T_c mechanism [2, 3], and spin fluctuation spectra were studied intensively in space of energy ω and momentum \mathbf{q} by inelastic neutron scattering already slightly after the discovery of high- T_c cuprates [4, 5]. Given that it is mobile electrons which form Cooper pairs, charge fluctuations should also be equally important to understand the high- T_c mechanism. In particular, the spin-charge stripe order [6] was observed in La-based cuprates around the hole doping $1/8$, where the superconductivity tends to be suppressed [7]. After the advent of resonance inelastic x-ray scattering (RIXS), charge excitations were investigated in much wider \mathbf{q} - ω space. There were two major discoveries. One was the charge ordering tendency, which is not accompanied by magnetic order in contrast to the spin-charge stripes, in the other hole-doped cuprates [8–16] as well as in electron-doped cuprates [17–19]. The charge order in electron-doped cuprates was explained in terms of d -wave bond-charge order [20–22], which is reduced to the electronic nematic order in the limit of zero momentum [23–25]. The origin of the charge order in the hole-doped cuprates is still controversial [26–33]. These spin and charge fluctuations were usually studied by focusing on the CuO_2 plane, namely, in a two-dimensional model with a short-range interaction.

The other distinguished discovery by RIXS was charge excitations close to the in-plane momentum $\mathbf{q}_{\parallel} = (0, 0)$. Their origin was discussed controversially in the early days [34–38], but they are now interpreted consistently as low-energy plasmon excitations with a gap at $\mathbf{q}_{\parallel} = (0, 0)$ that is scaled by weak interlayer hopping. In this sense, it may be referred to as acousticlike plasmons [36, 39–48]. Therefore, in contrast to usual analyses in a two-dimensional model with a short-range interaction, not only the long-range Coulomb interaction but also the three-dimensional layered structure has to be considered to understand the charge dynamics in cuprates. In particular, it was pointed out theoretically [36, 40] that their q_z dispersion is crucial to identify them as acousticlike plasmons. The acousticlike plasmons are realized for a finite q_z and become the conventional optical plasmon at $q_z = 0$ [49–51]. So far, those RIXS experiments have been performed mainly in single-layer cuprates, one CuO_2 plane per unit cell.

A natural question is whether such plasmon excitations can be universal in cuprate super-

conductors, especially for multilayer systems (multiple CuO_2 planes in the unit cell). This is particularly interesting because multilayer cuprates can exhibit T_c around 100 K, much higher than most of single-layer cuprates. Hence their charge dynamics may contain an important clue to understand the high- T_c mechanism. Recently, the RIXS experiments were performed for the bilayer cuprates $\text{YBa}_2\text{Cu}_3\text{O}_{6+\delta}$ and Ca-doped $\text{YBa}_2\text{Cu}_3\text{O}_{6+\delta}$ [52]. The data suggested a single plasmon mode, similar to that observed in the single-layer cuprates.

Meanwhile, there were theoretical studies of plasmons in a bilayer system by using the electron-gas model that incorporated the long-range Coulomb interaction (LRC) [53, 54]. In this model, electrons are mobile only inside the layer—no hopping between the layers—and electrons interact with each other via the LRC not only inside the layer but also in different layers. Griffin and Pindor [54] performed detailed and clear analysis in the context of cuprates. They predicted two plasmon modes, in-phase and out-of-phase modes between the two layers inside the unit cell, which we may call the ω_+ mode and ω_- mode, respectively, following Ref. [54]. The ω_+ mode bears a feature similar to plasmons in the single-layer system and the ω_- mode is a new feature in the bilayer system. Both ω_{\pm} modes were predicted to be gapless and the ω_- mode had a negligible q_z dependence and energy lower than the ω_+ mode [54]. In cuprates, however, it is expected that there is at least sizable intrabilayer hopping. Moreover, it is questionable whether the electron-gas model [53, 54] is applicable to materials close to half-filling such as cuprates and nickelates, which are usually regarded as electron-liquid systems—rather the electron-gas model has been applied typically to semiconductor superlattices [55]. Nonetheless, the formulae of the LRC obtained in the electron-gas model [53] were frequently employed even for systems far away from the low-electron density limit [39, 52, 54, 56, 57]. We infer that its reason may lie in capturing correctly the plasmon continuum specific to layered systems [53, 54, 58, 59] and the q^{-2} singularity of the LRC in the limit of $\mathbf{q} \rightarrow \mathbf{0}$, leading to plasmons, and in an expectation that the essential physics for the long-wavelength limit ($\mathbf{q} \rightarrow \mathbf{0}$) may be described in the electron-gas model.

The theoretical analysis in Ref. [52] fixed partially an apparent drawback of the electron-gas model by including the lattice structure in the kinetic term and also a finite intrabilayer hopping [60], yet keeping the same functional form of the LRC as that in the electron-gas model [53, 54]. Hence the serious drawbacks remain: i) the interaction term lost 2π periodicity inside the layer although the lattice structure was considered for the kinetic

term, ii) the charge excitation spectrum along the q_z direction was tacitly assumed to have 2π periodicity, which is not correct because the spectral weight loses such periodicity, and iii) RIXS experiments were usually performed in wide \mathbf{q} - ω space [34, 35, 37–39, 42, 43, 45–48], not restricted to the vicinity of $\mathbf{q}_{\parallel} = (0, 0)$ and $q_z c = 0$; in fact, $q_z c$ was frequently taken away from zero in many RIXS experiments [39, 42, 43, 45–48]. These features indicate some limitation of previous theoretical analyses [52, 54], which eventually may not be sustainable to a sound comparison with RIXS data especially for materials near half-filling. This is particularly serious since the charge dynamics in multi-layer cuprates, which exhibit T_c around 100 K, contains potentially some important hints to the understanding of the high-temperature superconducting mechanism.

Motivated by this possible importance, we shall derive formulae of the LRC beyond the ones obtained in the electron-gas model by Fetter 50 years ago [53]—we refer to it as the Fetter model—so that we can apply the formulae to a lattice system with any electron density. This was already achieved for the single-layer lattice model [36, 44, 61], but is largely unknown for multilayer electron systems. We shall consider a bilayer lattice model as the simplest case. But even in this simplest case, we are not aware of literature to develop the Fetter model. Such a development will eventually make it possible to achieve a detailed comparison between theory and experiments even far away from the low-electron density limit, especially for materials modeled by electron liquids such as cuprates, nickelates and others. Moreover, it may be historically important to construct a theory with the LRC applicable to any materials, independent of the electron density, by respecting the full lattice symmetry, for example in graphite [62, 63].

In this paper, we derive formulae of the LRC on a bilayer lattice by solving the Poisson equation and demonstrate its validity by checking various limits. Our obtained formulae are general and can be applicable to any bilayer square lattice systems, especially when one wishes to study the charge dynamics in the presence of the LRC; the extension to other lattice geometry is straightforward. Given the current interests in the charge dynamics in cuprates, we choose model parameters appropriate to cuprates, although strong correlation effects specific to cuprates are not taken into account. Rather we give weight to clarifying the characteristic feature of the charge dynamics in the bilayer lattice model with the LRC. The inclusion of the strong electron correlations in the context of the t - J - V model [36] and the further extension to three- and four-layer systems are left in the future.

The present manuscript is organized as follows. In Sec. II, we introduce a bilayer model with a density-density interaction. We then study the case of the LRC in Sec. II B. Equations (28) and (29) are the formulae beyond the Fetter model—one of the most important results in the present work. The analytical form of the dynamical charge susceptibility is presented in the non-interacting case, the bilayer case only with the intrabilayer hopping, and the most general case. Numerical results are presented in Sec. III. First we turn off the interbilayer hopping t'_z , clarify the overall charge-excitation spectrum, and elaborate the property of the ω_{\pm} modes. Next we introduce t'_z and show its major effect. In the discussion section (Sec. IV), we make a comparison with RIXS data, the Fetter model, and the case of a short-range interaction, and discuss a relation to charge ordering tendencies in cuprates. Conclusions are given in Sec. V. We also study the limit of the single-layer case in our formulae [Eqs. (28) and (29)] in Appendix A and clarify a fine structure of the ω_{\pm} modes at $q_z c = \pi$ in Appendix B.

II. FORMALISM

A. Hamiltonian

We consider an electron system interacting with the LRC on a bilayer square lattice stacked along the z axis with the intrabilayer distance d and interbilayer distance c as shown in Fig. 1; we can assume $0 < d \leq c/2$ without losing generality. The resulting Hamiltonian consists of two terms

$$\mathcal{H} = \mathcal{H}_0 + \mathcal{H}_I. \quad (1)$$

\mathcal{H}_0 describes the kinetic term and is given by

$$\mathcal{H}_0 = \sum_{\mathbf{k}, \sigma} \begin{pmatrix} c_{1\mathbf{k}\sigma}^\dagger & c_{2\mathbf{k}\sigma}^\dagger \end{pmatrix} \begin{pmatrix} \xi_{\mathbf{k}} & \varepsilon_{\mathbf{k}} e^{ik_z d} \\ \varepsilon_{\mathbf{k}}^* e^{-ik_z d} & \xi_{\mathbf{k}} \end{pmatrix} \begin{pmatrix} c_{1\mathbf{k}\sigma} \\ c_{2\mathbf{k}\sigma} \end{pmatrix}, \quad (2)$$

where $c_{1\mathbf{k}\sigma}^\dagger$ ($c_{2\mathbf{k}\sigma}^\dagger$) and $c_{1\mathbf{k}\sigma}$ ($c_{2\mathbf{k}\sigma}$) are creation and annihilation operators of electrons with momentum \mathbf{k} and spin σ on the layer 1 (2); $\xi_{\mathbf{k}}$ and $\varepsilon_{\mathbf{k}}$ are the in-plane and out-of-plane dispersions, respectively, and are given by

$$\xi_{\mathbf{k}} = -2t(\cos k_x a + \cos k_y a) - 4t' \cos k_x a \cos k_y a - 2t''(\cos 2k_x a + \cos 2k_y a) - \mu, \quad (3)$$

$$\varepsilon_{\mathbf{k}} = \varepsilon_{\mathbf{k}}^\perp + \varepsilon_{\mathbf{k}}^{\perp'} e^{-ik_z c}. \quad (4)$$

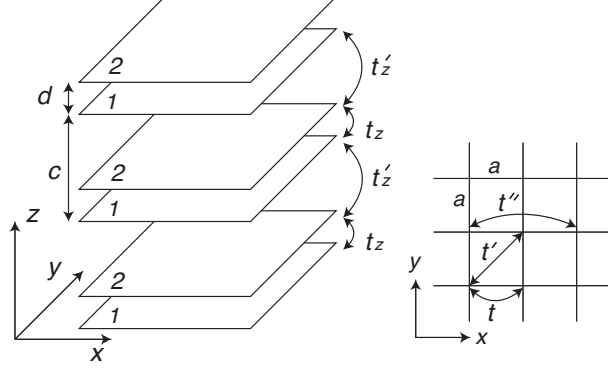


FIG. 1. Bilayer model. Each layer forms a square lattice and the hopping integrals are considered up to the third nearest-neighbor sites, t , t' , and t'' (right figure). The unit cell contains two layers, 1 and 2. The intrabilayer hopping is given by t_z and the interbilayer hopping is t'_z . The lattice constants are given by a , a and c along the x , y , and z directions, respectively, and the intrabilayer distance is $d(\leq c/2)$.

The hopping integrals t_z and t'_z between the layers (see Fig. 1) yield the dispersions $\varepsilon_{\mathbf{k}}^\perp$ and $\varepsilon_{\mathbf{k}}^{\perp'}$, respectively,

$$\varepsilon_{\mathbf{k}}^\perp = -t_z(\cos k_x a - \cos k_y a)^2, \quad (5)$$

$$\varepsilon_{\mathbf{k}}^{\perp'} = -t'_z(\cos k_x a - \cos k_y a)^2. \quad (6)$$

The form factor $\cos k_x a - \cos k_y a$ is expected in local density approximation (LDA) band calculations [64].

The lattice sites in the layer 1 in Fig. 1 are specified by $\mathbf{r}_i = n_x a \hat{\mathbf{x}} + n_y a \hat{\mathbf{y}} + n_z c \hat{\mathbf{z}}$ with the unit vectors $\hat{\mathbf{x}}$, $\hat{\mathbf{y}}$, and $\hat{\mathbf{z}}$ along the x , y , and z directions, respectively, and with integers n_x , n_y , and n_z . The lattice sites on the layer 2 are then described by $\mathbf{r}_i + \mathbf{d}$ with $\mathbf{d} = (0, 0, d)$. Hence in real space, the density-density interaction is given by

$$\begin{aligned} H_I = \frac{1}{2} \sum_{ij} [& n_1(\mathbf{r}_i) V(\mathbf{r}_j - \mathbf{r}_i) n_1(\mathbf{r}_j) \\ & + n_2(\mathbf{r}_i + \mathbf{d}) V(\mathbf{r}_j - \mathbf{r}_i) n_2(\mathbf{r}_j + \mathbf{d}) \\ & + n_1(\mathbf{r}_i) V(\mathbf{r}_j + \mathbf{d} - \mathbf{r}_i) n_2(\mathbf{r}_j + \mathbf{d}) \\ & + n_2(\mathbf{r}_i + \mathbf{d}) V(\mathbf{r}_j - \mathbf{r}_i - \mathbf{d}) n_1(\mathbf{r}_j)] . \end{aligned} \quad (7)$$

After the Fourier transform,

$$n_1(\mathbf{r}_i) = \frac{1}{N} \sum_{\mathbf{q}} n_1(\mathbf{q}) e^{i\mathbf{q} \cdot \mathbf{r}_i}, \quad (8)$$

$$n_2(\mathbf{r}_i + \mathbf{d}) = \frac{1}{N} \sum_{\mathbf{q}} n_2(\mathbf{q}) e^{i\mathbf{q} \cdot (\mathbf{r}_i + \mathbf{d})}, \quad (9)$$

we obtain

$$\mathcal{H}_I = \frac{1}{2N} \sum_{\mathbf{q}} \begin{pmatrix} n_1(\mathbf{q}) & n_2(\mathbf{q}) \end{pmatrix} \begin{pmatrix} V(\mathbf{q}) & V'(\mathbf{q}) \\ V'(-\mathbf{q}) & V(\mathbf{q}) \end{pmatrix} \begin{pmatrix} n_1(-\mathbf{q}) \\ n_2(-\mathbf{q}) \end{pmatrix}, \quad (10)$$

where N is the total number of lattice sites; $n_1(\mathbf{q}) = \sum_{\mathbf{k}, \sigma} c_{1\mathbf{k}\sigma}^\dagger c_{1\mathbf{k}+\mathbf{q}\sigma}$ and $n_2(\mathbf{q}) = \sum_{\mathbf{k}, \sigma} c_{2\mathbf{k}\sigma}^\dagger c_{2\mathbf{k}+\mathbf{q}\sigma}$ are the electron density operators of the momentum \mathbf{q} in each layer; the Fourier transform of the interaction part is given by

$$V(\mathbf{l}) = \frac{1}{N} \sum_{\mathbf{q}} V(\mathbf{q}) e^{i\mathbf{q} \cdot \mathbf{l}}, \quad (11)$$

$$V(\mathbf{l} + \mathbf{d}) = \frac{1}{N} \sum_{\mathbf{q}} V'(\mathbf{q}) e^{i\mathbf{q} \cdot (\mathbf{l} + \mathbf{d})}, \quad (12)$$

with $\mathbf{l} = \mathbf{r}_j - \mathbf{r}_i$.

B. LRC on bilayer lattice

Equation (10) is applicable to any density-density interaction. In particular, we consider the LRC in the present study. See Sec. IV C for the case of a short-range interaction, which is much simpler than the case of the LRC.

Needless to say, the functional factor of $V(\mathbf{l})$ corresponds to the well-known LRC $V(\mathbf{l}) \propto \frac{e^2}{|\mathbf{l}|}$ in continuum space and e is the electric charge; its Fourier transform is given by $\sim \frac{e^2}{q^2}$. If one is interested in the vicinity of momentum $\mathbf{q} = \mathbf{0}$, such a functional form could be justified to be employed even on a lattice system; at least, the singularity of the LRC is correctly captured. However, the asymptotic form in a bilayer system is not correctly reproduced as we point it out in Sec. IV B. Moreover, typically RIXS measurements are performed at \mathbf{q} away from zero to avoid a very strong elastic signal that masks the low-energy charge excitations [34, 35, 37–39, 42, 43, 45–48]. Therefore, it is requisite to use the LRC that respects the lattice structure. It is already known how to compute the LRC on a Bravais lattice [61], but we are not aware of literature to provide expressions of $V(\mathbf{q})$ and $V'(\mathbf{q})$ for the bilayer, more

generally multilayer, case beyond the 50-year-old model by Fetter [53, 54]. In fact, we have recognized that the derivation of the LRC on a multilayer system is not straightforward at all. We therefore focus on the bilayer case in the present work and elucidate characteristic features of the charge dynamics in the presence of the LRC, which contains enough insights beyond the available knowledge [54].

To obtain the LRC on a lattice, the standard procedure is to solve the Poisson equation as demonstrated in Ref. [61] for the single-layer case. We start from the Poisson equation with spatial anisotropy:

$$\epsilon_{\parallel} \left(\frac{\partial^2}{\partial x^2} + \frac{\partial^2}{\partial y^2} \right) G(\mathbf{r}) + \epsilon_{\perp} \frac{\partial^2}{\partial z^2} G(\mathbf{r}) = -\delta(\mathbf{r}), \quad (13)$$

where $\epsilon_{\parallel}(\epsilon_{\perp})$ is the dielectric constant parallel (perpendicular) to the layer. On the lattice, the second differential is replaced by the difference

$$\begin{aligned} & \frac{\epsilon_{\parallel}}{a^2} \{ [G(\mathbf{r}_i + a\hat{\mathbf{x}}) - 2G(\mathbf{r}_i) + G(\mathbf{r}_i - a\hat{\mathbf{x}})] \\ & \quad + [G(\mathbf{r}_i + a\hat{\mathbf{y}}) - 2G(\mathbf{r}_i) + G(\mathbf{r}_i - a\hat{\mathbf{y}})] \} \\ & + \epsilon_{\perp} [h_1 G(\mathbf{r}_i + c\hat{\mathbf{z}}) + h_2 G(\mathbf{r}_i + d\hat{\mathbf{z}}) + h_3 G(\mathbf{r}_i) + h_4 G(\mathbf{r}_i - (c-d)\hat{\mathbf{z}})] \\ & = -\frac{1}{N} \sum_{\mathbf{q}} e^{i\mathbf{q}\cdot\mathbf{r}_i}. \end{aligned} \quad (14)$$

Here we use 4 points to evaluate $\frac{\partial^2 G(\mathbf{r})}{\partial z^2}$ so that the equation is valid even for $d = 0$; the coefficients are determined uniquely by the Taylor expansion, yielding

$$h_1 = \frac{2(c-2d)}{c(2c-d)(c-d)}, \quad (15)$$

$$h_2 = \frac{2}{c(c-d)}, \quad (16)$$

$$h_3 = -\frac{4}{c(c-d)}, \quad (17)$$

$$h_4 = \frac{2(c+d)}{c(2c-d)(c-d)}. \quad (18)$$

From the Fourier transform defined in Eqs. (11) and (12), we obtain

$$\begin{aligned} & \left[\frac{2\epsilon_{\parallel}}{a^2} (2 - \cos q_x a - \cos q_y a) - \epsilon_{\perp} (h_1 e^{iq_z c} + h_3) \right] G(\mathbf{q}) \\ & - \epsilon_{\perp} e^{iq_z d} (h_2 + h_4 e^{-iq_z c}) G'(\mathbf{q}) = 1. \end{aligned} \quad (19)$$

Note that $G'(\mathbf{q})$ appears in the second line, suggesting a necessity of two independent equa-

tions. The other Poisson equation on a bilayer lattice may be considered at $\mathbf{r} + \mathbf{d}$ in Eq. (13):

$$\begin{aligned} & \frac{\epsilon_{\parallel}}{a^2} \{ [G(\mathbf{r}_i + \mathbf{d} + a\hat{\mathbf{x}}) - 2G(\mathbf{r}_i + \mathbf{d}) + G(\mathbf{r}_i + \mathbf{d} - a\hat{\mathbf{x}})] \\ & \quad + [G(\mathbf{r}_i + \mathbf{d} + a\hat{\mathbf{y}}) - 2G(\mathbf{r}_i + \mathbf{d}) + G(\mathbf{r}_i + \mathbf{d} - a\hat{\mathbf{y}})] \} \\ & + \epsilon_{\perp} [h_5 G(\mathbf{r}_i + c\hat{\mathbf{z}}) + h_6 G(\mathbf{r}_i + d\hat{\mathbf{z}}) + h_7 G(\mathbf{r}_i) + h_8 G(\mathbf{r}_i - (c - d)\hat{\mathbf{z}})] \\ & = 0. \end{aligned} \quad (20)$$

The right hand side becomes zero because $\delta(\mathbf{r}_i + \mathbf{d}) = 0$ in the condition $0 < d \leq c/2$. When we determine the coefficients h_5, h_6, h_7, h_8 by the Taylor expansion, we find that $h_5 = h_4$, $h_6 = h_3$, $h_7 = h_2$, and $h_8 = h_1$. We then obtain

$$\begin{aligned} & \left[\frac{2\epsilon_{\parallel}}{a^2} (2 - \cos q_x a - \cos q_y a) - \epsilon_{\perp} (h_1 e^{-iq_z c} + h_3) \right] G'(\mathbf{q}) \\ & - \epsilon_{\perp} e^{-iq_z d} (h_2 + h_4 e^{iq_z c}) G(\mathbf{q}) = 0. \end{aligned} \quad (21)$$

Equations (19) and (21) are reduced to a 2×2 matrix equation

$$\begin{pmatrix} A_{11} & A_{12} \\ A_{12}^* & A_{11}^* \end{pmatrix} \begin{pmatrix} G(\mathbf{q}) \\ G'(\mathbf{q}) \end{pmatrix} = \begin{pmatrix} 1 \\ 0 \end{pmatrix}, \quad (22)$$

where

$$A_{11} = \frac{2\epsilon_{\parallel}}{a^2} (2 - \cos q_x a - \cos q_y a) - \epsilon_{\perp} (h_1 e^{iq_z c} + h_3), \quad (23)$$

$$A_{12} = -\epsilon_{\perp} e^{iq_z d} (h_2 + h_4 e^{-iq_z c}). \quad (24)$$

Hence we obtain the solution of the Poisson equation for the bilayer system in momentum space as

$$G(\mathbf{q}) = \frac{A_{11}^*}{|A_{11}|^2 - |A_{12}|^2}, \quad (25)$$

$$G'(\mathbf{q}) = \frac{-A_{12}^*}{|A_{11}|^2 - |A_{12}|^2}. \quad (26)$$

The above solution is related to the LRC via

$$V(\mathbf{q}) = \frac{e^2}{a^2 c} \text{Re} G(\mathbf{q}), \quad V'(\mathbf{q}) = \frac{e^2}{a^2 c} G'(\mathbf{q}), \quad (27)$$

where the factor $1/(a^2 c)$ comes from the volume of the unit cell. The diagonal component of $V(\mathbf{q})$ is given by the real part of $G(\mathbf{q})$. This is because only the even term with respect to \mathbf{q}

contributes to the diagonal part of the interaction in Eq. (10)—the term $\sin q_z c$ originating from Eq. (23) is canceled out.

It may be convenient to present the explicit expressions of $V(\mathbf{q})$ and $V'(\mathbf{q})$, which are computed as:

$$V(\mathbf{q}) = \frac{V_c}{\det \tilde{V}} \left[\alpha(2 - \cos q_x a - \cos q_y a) - \frac{1}{2} \tilde{h}_3 - \frac{1}{2} \tilde{h}_1 \cos q_z c \right], \quad (28)$$

$$V'(\mathbf{q}) = \frac{1}{2} \frac{V_c}{\det \tilde{V}} \left[\tilde{h}_2 \cos q_z d + \tilde{h}_4 \cos q_z (c - d) - i \tilde{h}_2 \sin q_z d + i \tilde{h}_4 \sin q_z (c - d) \right], \quad (29)$$

$$\det \tilde{V} = [\alpha(2 - \cos q_x a - \cos q_y a)]^2 - \alpha(2 - \cos q_x a - \cos q_y a)(\tilde{h}_1 \cos q_z c + \tilde{h}_3) + \frac{6c^2}{(c - d)(2c - d)}(1 - \cos q_z c). \quad (30)$$

Here $\tilde{h}_i = c^2 h_i$ with $i = 1, 2, 3, 4$ is a dimensionless factor given in Eqs. (15)–(18); $V_c = \frac{e^2 c}{2a^2 \epsilon_\perp}$ and $\alpha = \frac{c^2 \epsilon_\parallel}{a^2 \epsilon_\perp}$, which are the same notations as those in the single-layer case [40, 41, 43, 45, 47, 48, 65]; V_c has the dimension of energy and so do $V(\mathbf{q})$ and $V'(\mathbf{q})$; α describes the anisotropy between the in-plane direction and the perpendicular direction.

C. Dynamical charge susceptibility

As shown in Eqs. (2) and (10), the Hamiltonian is described by a 2×2 matrix. Thus the charge susceptibility $\kappa_{ij}(\mathbf{q}, \omega)$ is also described by a 2×2 matrix. We compute κ_{ij} in the random phase approximation (RPA), yielding

$$\kappa_{ij}(\mathbf{q}, \omega) = \kappa_{ij}^0(\mathbf{q}, \omega) + \sum_{l_1, l_2} \kappa_{il_1}^0(\mathbf{q}, \omega) V_{l_1 l_2}(\mathbf{q}) \kappa_{l_2 j}(\mathbf{q}, \omega), \quad (31)$$

where $i, j, l_1, l_2 = 1$ and 2 ; $\kappa_{ij}^0(\mathbf{q}, \omega)$ describes a simple bubble diagram and is computed as

$$\kappa_{11}^0(\mathbf{q}, \omega) = \frac{1}{2N} \sum_{\mathbf{k}} (g_{++} + g_{+-} + g_{-+} + g_{--}), \quad (32)$$

$$\kappa_{12}^0(\mathbf{q}, \omega) = \frac{1}{2N} \sum_{\mathbf{k}} \frac{\varepsilon_{\mathbf{k}} \varepsilon_{\mathbf{k}+\mathbf{q}}^* e^{-iq_z d}}{|\varepsilon_{\mathbf{k}}| |\varepsilon_{\mathbf{k}+\mathbf{q}}|} (g_{++} - g_{+-} - g_{-+} + g_{--}), \quad (33)$$

$$\kappa_{21}^0(\mathbf{q}, \omega) = \frac{1}{2N} \sum_{\mathbf{k}} \frac{\varepsilon_{\mathbf{k}}^* \varepsilon_{\mathbf{k}+\mathbf{q}} e^{iq_z d}}{|\varepsilon_{\mathbf{k}}| |\varepsilon_{\mathbf{k}+\mathbf{q}}|} (g_{++} - g_{+-} - g_{-+} + g_{--}), \quad (34)$$

$$\kappa_{22}^0(\mathbf{q}, \omega) = \kappa_{11}^0(\mathbf{q}, \omega), \quad (35)$$

where \mathbf{k} is defined in the first Brillouin zone and we omit the arguments on the right hand side in $g_{\mu\nu}$ with $\mu, \nu = +$ and $-$, which are given by

$$g_{\mu\nu}(\mathbf{k}, \mathbf{q}, \omega) = \frac{f(\lambda_\mu(\mathbf{k})) - f(\lambda_\nu(\mathbf{k} + \mathbf{q}))}{\lambda_\mu(\mathbf{k}) + \omega + i\Gamma - \lambda_\nu(\mathbf{k} + \mathbf{q})}. \quad (36)$$

$f(x)$ is the Fermi distribution function, the eigenenergies $\lambda_{\pm}(\mathbf{k}) = \xi_{\mathbf{k}} \pm |\varepsilon_{\mathbf{k}}|$ describe the antibonding and bonding bands, respectively [see Eqs. (3) and (4)], and $\Gamma(> 0)$ is an infinitesimally small value, but we shall take a finite value for numerical convenience, which may mimics to some extent broadening effects not included in the RPA. Each component of $V_{l_1 l_2}$ in Eq. (31) is given by the component of the matrix in Eq. (10). The total susceptibility is then given by

$$\kappa(\mathbf{q}, \omega) = \frac{1}{2} \sum_{ij} \kappa_{ij}(\mathbf{q}, \omega) \quad (37)$$

While Eq. (37) is a compact form, it may be more insightful to present an explicit form of $\kappa(\mathbf{q}, \omega)$.

1. Non-interacting case for $t'_z = 0$

We first consider the non-interacting charge susceptibility $\kappa^0(\mathbf{q}, \omega)$:

$$\kappa^0(\mathbf{q}, \omega) = \frac{1}{2} [\kappa_{11}^0(\mathbf{q}, \omega) + \kappa_{12}^0(\mathbf{q}, \omega) + \kappa_{21}^0(\mathbf{q}, \omega) + \kappa_{22}^0(\mathbf{q}, \omega)] \quad (38)$$

$$= \cos^2 \frac{q_z d}{2} \kappa_{\text{even}}^0(\mathbf{q}, \omega) + \sin^2 \frac{q_z d}{2} \kappa_{\text{odd}}^0(\mathbf{q}, \omega), \quad (39)$$

where

$$\kappa_{\text{even}}^0(\mathbf{q}, \omega) = \frac{1}{N} \sum_{\mathbf{k}} (g_{++} + g_{--}), \quad (40)$$

$$\kappa_{\text{odd}}^0(\mathbf{q}, \omega) = \frac{1}{N} \sum_{\mathbf{k}} (g_{+-} + g_{-+}), \quad (41)$$

and $\kappa_{\text{even(odd)}}^0(\mathbf{q}, \omega)$ is the susceptibility from the intraband (interband) scattering processes and thus is frequently called the even (odd) mode in a bilayer system. The even and odd modes are selected by choosing $q_z d = 0$ and π , respectively.

2. Bilayer model with LRC for $t'_z = 0$

Next we introduce the LRC, which yields both intra- and interbilayer interactions, although the hopping along the z direction is restricted only within the intrabilayer. We then obtain

$$\begin{aligned} \kappa(\mathbf{q}, \omega) = \frac{1}{\text{det}} \left[\cos^2 \frac{q_z d}{2} \kappa_{\text{even}}^0(\mathbf{q}, \omega) + \sin^2 \frac{q_z d}{2} \kappa_{\text{odd}}^0(\mathbf{q}, \omega) \right. \\ \left. - \kappa_{\text{even}}^0(\mathbf{q}, \omega) \kappa_{\text{odd}}^0(\mathbf{q}, \omega) V''(\mathbf{q}) \right], \end{aligned} \quad (42)$$

where

$$\begin{aligned} \mathfrak{det} &= [1 - (V(\mathbf{q}) + V_+(\mathbf{q})) \kappa_{\text{even}}^0(\mathbf{q}, \omega)] \\ &\times [1 - (V(\mathbf{q}) - V_+(\mathbf{q})) \kappa_{\text{odd}}^0(\mathbf{q}, \omega)] \\ &+ \kappa_{\text{even}}^0(\mathbf{q}, \omega) \kappa_{\text{odd}}^0(\mathbf{q}, \omega) V_-(\mathbf{q})^2. \end{aligned} \quad (43)$$

$$V''(\mathbf{q}) = V(\mathbf{q}) - \frac{V'(\mathbf{q}) + V'(-\mathbf{q})}{2}, \quad (44)$$

$$V_{\pm}(\mathbf{q}) = \frac{V'(\mathbf{q})e^{iq_z d} \pm V'(-\mathbf{q})e^{-iq_z d}}{2}. \quad (45)$$

It is insightful to compare Eq. (42) with Eq. (39). The charge susceptibility can still be described in terms of κ_{even}^0 and κ_{odd}^0 in Eq. (42), but in contrast to Eq. (39), they cannot be fully decoupled from each other in general. This is because the LRC yields the interbilayer interaction and thus we have an additional term $\kappa_{\text{even}}^0 \kappa_{\text{odd}}^0 V''(\mathbf{q})$ in the numerator and two terms in the denominator that describe couplings of κ_{even}^0 and κ_{odd}^0 . Hence the even and odd modes are no longer good quantities to specify the charge excitations. This is in a sharp contrast to the case of a short-range interaction; see Sec. IV C. Nonetheless there are exceptions. i) The even mode is well defined at $q_z c = 0$ [see Eqs. (60) and (61)] because the ω_- mode vanishes at any q_{\parallel} . ii) The odd mode is well defined at specific points $\mathbf{q}_{\parallel} = (0, 0)$ and $q_z c = 2n\pi$ with $n \neq 0$, where the ω_+ mode has zero intensity [see Figs. 3(e), 5(e), and 7(e)].

The origin of \mathfrak{det} in Eq. (43) is readily understood. The RPA susceptibility Eq. (31) is written in a 2×2 matrix form

$$\hat{\kappa} = \hat{\kappa}^0 + \hat{\kappa}^0 \hat{V} \hat{\kappa}, \quad (46)$$

where \hat{V} corresponds to the interaction matrix given in Eq. (10). We then obtain

$$\hat{\kappa} = (1 - \hat{\kappa}^0 \hat{V})^{-1} \hat{\kappa}^0. \quad (47)$$

\mathfrak{det} in Eq. (43) is given by

$$\mathfrak{det} = \det(1 - \hat{\kappa}^0 \hat{V}). \quad (48)$$

The charge excitation spectrum is studied by $\text{Im}\kappa(\mathbf{q}, \omega)$ in \mathbf{q} - ω space in Eq. (42). As expected, plasmons can be realized when the condition $\mathfrak{det} = 0$ is fulfilled. Hence we may also analyze Eq. (48) in the present study. For numerical convenience, however, we may study the minimum value of $|\mathfrak{det}|$ because of a possible mixture of the continuum spectrum in actual calculations.

3. Bilayer model with LRC and t'_z

As shown in Eq. (42), we can still extract κ_{even}^0 and κ_{odd}^0 without t'_z , even though they are not good quantities. However, once t'_z is included, they are not extracted in a convenient way and we obtain:

$$\kappa(\mathbf{q}, \omega) = \frac{\kappa_{11}^0 + \kappa_{\text{cos}}^0 - [(\kappa_{11}^0)^2 - (\kappa_{\text{cos}}^0)^2 - (\kappa_{\text{sin}}^0)^2][V(\mathbf{q}) - V'_+(\mathbf{q})]}{\mathfrak{d}\mathfrak{e}\mathfrak{t}}, \quad (49)$$

$$\mathfrak{d}\mathfrak{e}\mathfrak{t} = 1 - 2\kappa_{11}^0 V(\mathbf{q}) - 2\kappa_{\text{cos}}^0 V'_+(\mathbf{q}) + i2\kappa_{\text{sin}}^0 V'_-(\mathbf{q}) \\ + [(\kappa_{11}^0)^2 - (\kappa_{\text{cos}}^0)^2 - (\kappa_{\text{sin}}^0)^2][V(\mathbf{q})^2 - V'(\mathbf{q})V'(-\mathbf{q})], \quad (50)$$

$$V'_\pm(\mathbf{q}) = \frac{1}{2}[V'(\mathbf{q}) \pm V'(-\mathbf{q})], \quad (51)$$

where $\mathfrak{d}\mathfrak{e}\mathfrak{t}$ is given by Eq. (48) with a finite t'_z , and we omit the arguments in κ_{11}^0 , κ_{cos}^0 , and κ_{sin}^0 for brevity. The last expression $V'_\pm(\mathbf{q})$ should not be mixed up with $V_\pm(\mathbf{q})$ in Eq. (45). κ_{cos}^0 and κ_{sin}^0 originate from the factor $\varepsilon_{\mathbf{k}}\varepsilon_{\mathbf{k}+\mathbf{q}}^*e^{iq_z d}$ and its conjugate in Eqs. (33) and (34), and are given by

$$\kappa_{\text{cos}}^0(\mathbf{q}, \omega) = \frac{1}{2N} \sum_{\mathbf{k}} \cos \varphi_{\mathbf{k}\mathbf{k}+\mathbf{q}} (g_{++} - g_{+-} - g_{-+} + g_{--}), \quad (52)$$

$$\kappa_{\text{sin}}^0(\mathbf{q}, \omega) = \frac{1}{2N} \sum_{\mathbf{k}} \sin \varphi_{\mathbf{k}\mathbf{k}+\mathbf{q}} (g_{++} - g_{+-} - g_{-+} + g_{--}). \quad (53)$$

Here

$$\varphi_{\mathbf{k}\mathbf{k}+\mathbf{q}} = \theta_{\mathbf{k}} - \theta_{\mathbf{k}+\mathbf{q}} - q_z d \quad (54)$$

and $\theta_{\mathbf{k}}$ comes from the hopping along the z direction,

$$\varepsilon_{\mathbf{k}} = |\varepsilon_{\mathbf{k}}|e^{i\theta_{\mathbf{k}}}, \quad (55)$$

$$|\varepsilon_{\mathbf{k}}| = \sqrt{(\varepsilon_{\mathbf{k}}^\perp + \varepsilon_{\mathbf{k}}^{\perp'} \cos k_z c)^2 + (\varepsilon_{\mathbf{k}}^{\perp'} \sin k_z c)^2}. \quad (56)$$

Although κ_{even}^0 and κ_{odd}^0 do not appear in Eq. (49), one can check that Eq. (49) is reduced to Eq. (42) by setting $t'_z = 0$ as it should be.

III. RESULTS

A choice of our model parameters is arbitrary and may depend on a target material. Since we wish to make a comparison with recent experimental data of bilayer cuprate high-temperature superconductors [52], we choose the following parameter set to achieve a reasonable comparison: $t'/t = -0.30$, $t''/t = 0.15$, $d/c = 3.36/11.68$ [52], $n = 0.79$, $V_c/t = 130$,

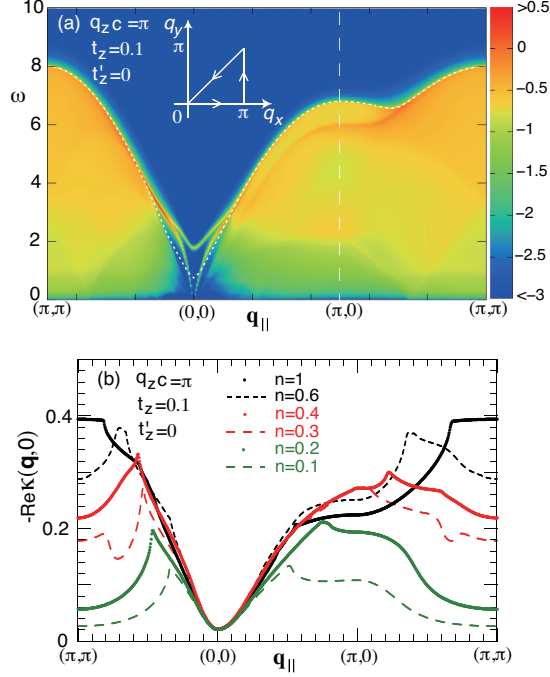


FIG. 2. (a) Intensity map of $\log_{10} |\text{Im}\kappa(\mathbf{q}, \omega)|$ along the symmetry directions shown in the inset; the long-dashed line specifies the position of $(\pi, 0)$. The white dotted curve is the upper boundary of the particle-hole excitations. Around $\mathbf{q}_{||} = (0, 0)$, there are two collective charge excitation modes, which are plasmons. The lower-energy one becomes gapless at $\mathbf{q}_{||} = (0, 0)$. (b) Real part of the static charge susceptibility along the symmetry directions for several choices of the electron density.

$\alpha = 40$, $\Gamma/t = 0.01$, and $T/t = 0.01$ in most of cases; n is the electron density. Since we will study t_z and t'_z dependencies, those values are always specified when we present results. We first study the case of $t'_z = 0$ (see Fig. 1). In this case, the electronic motion is restricted within the bilayer, but the electrons interact with each other via the LRC between different layers. The effect of t'_z shall be clarified later. We use t as the unit of energy and put $t = 1$ below. We also put the in-plane lattice constant $a = 1$ for brevity.

A. Charge excitation spectra with $t'_z = 0$

1. Overall features

Figure 2(a) is the intensity map of $\text{Im}\kappa(\mathbf{q}, \omega)$ along the symmetry directions (π, π) – $(0, 0)$ – $(\pi, 0)$ – (π, π) as seen in the inset; $q_z c = \pi$ is taken. The white dotted curve is the upper boundary of the particle-hole continuum excitations. Note that low-energy continuum excitations are present even at $\mathbf{q}_{\parallel} = (0, 0)$, because of a finite t_z . Inside the continuum spectrum, relatively large spectral weight spreads broadly in a high-energy region and the spectral weight tends to be suppressed at lower energy. Above the continuum spectrum around $\mathbf{q}_{\parallel} = (0, 0)$, there are two collective charge modes, which are plasmons.

In Fig. 2(b) we plot the real part of the static charge susceptibility for various choices of the electron density, confirming no charge ordering tendency. Although a peak structure forms along the $(0, 0)$ – (π, π) direction especially at low density, the susceptibility itself becomes smaller with decreasing the density—it cannot be associated with a potential charge ordering such as a Wigner crystallization [66] in the present bilayer square lattice system.

2. Maps of the spectral weight

Having made sure of no charge ordering in the present model, we focus on collective charge excitations around $\mathbf{q}_{\parallel} = (0, 0)$ realized above the upper boundary of the particle-hole excitations in Fig. 2. These are plasmon excitations characterized by two modes. Following Ref. [54], we may call the upper and lower branches as the ω_+ mode and ω_- mode, respectively, although we will show later that the energy of the ω_{\pm} modes is interchanged for a large t_z .

Figures 3(a)–(e) show \mathbf{q} – ω maps focusing on plasmon excitations around $\mathbf{q}_{\parallel} = (0, 0)$ for a sequence of $q_z c$. The square of the modulus of the denominator of Eq. (42), namely Eq. (48) is also shown on the right hand side of Fig. 3. At $q_z c = 0$ [Fig. 3(a)], there exists the ω_+ mode only—the optical plasmon mode—and no ω_- mode is realized. This is easily understood.

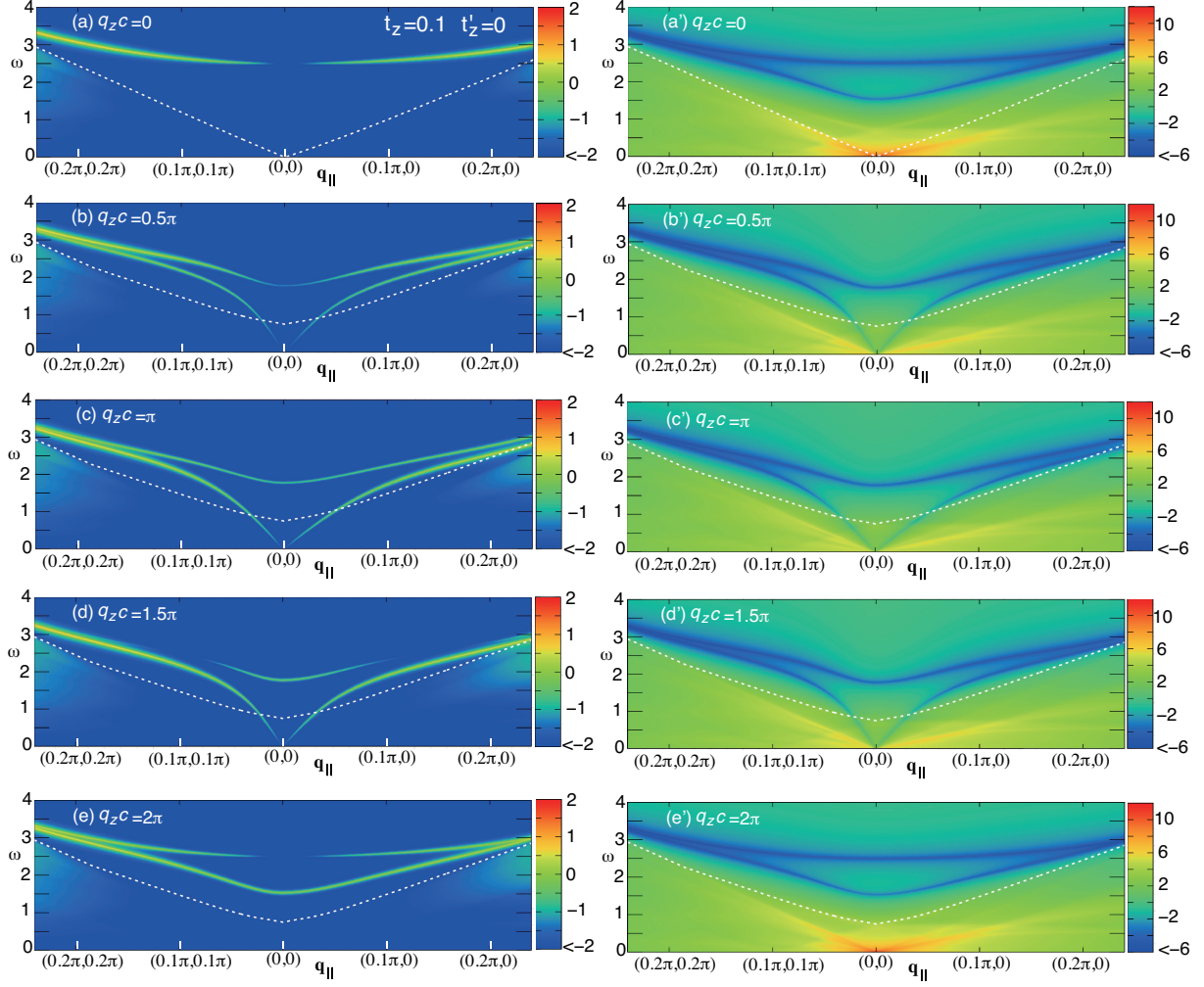


FIG. 3. Intensity map of $\log_{10}|\text{Im}\kappa(\mathbf{q}, \omega)|$ (left panels) and $\log_{10}|\det|^2$ given in Eq. (42) (right panels) for a sequence of $q_z c$ around a region of $\mathbf{q}_{||} = (0, 0)$: (a) and (a') $q_z c = 0$, (b) and (b') $q_z c = 0.5\pi$, (c) and (c') $q_z c = \pi$, (d) and (d') $q_z c = 1.5\pi$, and (e) and (e') $q_z c = 2\pi$. The white dotted curve denotes the upper boundary of the particle-hole continuum. It goes to zero at $\mathbf{q}_{||} = (0, 0)$ and $q_z c = 0$ even for a finite $t_z = 0.1$. To keep an appropriate contrast, the same color is used below -2 and -6 in the left panels and the right panels, respectively.

Equations (44) and (45) show at $q_z c = 0$

$$V''(\mathbf{q}) = V(\mathbf{q}) - V'(\mathbf{q}), \quad (57)$$

$$V_+(\mathbf{q}) = V'(\mathbf{q}), \quad (58)$$

$$V_-(\mathbf{q}) = 0. \quad (59)$$

From Eq. (42) we then obtain

$$\kappa(\mathbf{q}, \omega) = \frac{\kappa_{\text{even}}^0(\mathbf{q}, \omega)[1 - \kappa_{\text{odd}}^0(\mathbf{q}, \omega)V''(\mathbf{q})]}{[1 - \kappa_{\text{even}}^0(\mathbf{q}, \omega)(V(\mathbf{q}) + V'(\mathbf{q}))][1 - \kappa_{\text{odd}}^0(\mathbf{q}, \omega)(V(\mathbf{q}) - V'(\mathbf{q}))]}, \quad (60)$$

$$= \frac{\kappa_{\text{even}}^0(\mathbf{q}, \omega)}{1 - \kappa_{\text{even}}^0(\mathbf{q}, \omega)(V(\mathbf{q}) + V'(\mathbf{q}))}. \quad (61)$$

That is, the ω_+ mode corresponds to the even mode at $q_z c = 0$. Since $\kappa_{\text{even}}^0 = 0$ at $\mathbf{q}_{\parallel} = (0, 0)$ and $q_z c = 0$ for finite ω , the intensity of the ω_+ mode vanishes at $\mathbf{q}_{\parallel} = (0, 0)$. Physically this implies that the ω_+ mode is in-phase inside the bilayer and thus cannot have spectral weight at $\mathbf{q}_{\parallel} = (0, 0)$ and $q_z c = 0$ because of the charge conservation—the other mode, namely the ω_- mode, therefore, should be out-of-phase charge-excitation mode in the bilayer system. This assignment is consistent with Ref. [54]. However, this argument is valid only at $q_z c = 0$. The relative motion of electrons between the two layers inside the unit cell becomes less trivial as going away from $q_z c = 0$. In fact, mathematically the in-phase or out-of-phase motion can be confirmed at $q_z c = 0$ by studying the eigenvector of the susceptibility matrix [Eq. (47)] at \mathbf{q}_{\parallel} and ω where Eq. (48) vanishes and such a result changes as varying $q_z c$ from zero.

Although there is no spectral weight at $\mathbf{q}_{\parallel} = (0, 0)$ and $q_z c = 0$ at any t_z , the presence of t_z yields low-energy spectral weight at $\mathbf{q}_{\parallel} = (0, 0)$ at $q_z c \neq 0$ and the upper boundary of the continuum spectrum has a finite energy. Above the continuum, we have two modes: the ω_+ mode and the ω_- mode for a higher- and lower-energy branch, respectively [54], as shown in Figs. 3(b)–(d). These modes should not be confused with the even and odd modes specific to a bilayer system, because the LRC yields the interaction among all layers as seen from Eq. (42) and the even and odd modes couple to each other. In particular, the ω_- mode shows the gapless dispersion, which may be clear when we recognize that the ω_- mode extends into the continuum spectrum around $\mathbf{q}_{\parallel} = (0, 0)$. At $q_z c = 2n\pi$ in Fig. 3(e), however, the ω_- mode becomes gapped. The ω_+ mode loses the spectral weight at $\mathbf{q}_{\parallel} = (0, 0)$, which is due to the property $\kappa_{\text{even}}^0 = 0$ there at $q_z c = 2n\pi$. A comparison between Figs. 3(a) and (e) highlights that the plasmon excitations at $q_z c = 0$ are not generic. Rather those at $q_z c = 2n\pi$ with $n \neq 0$ are generic: both ω_{\pm} modes are present and the intensity of the ω_+ mode vanishes at $\mathbf{q}_{\parallel} = (0, 0)$ whereas it does not for the ω_- mode.

The gapless feature of the ω_- mode is highlighted in Figs. 4(a)–(c) by focusing on the vicinity of $\mathbf{q}_{\parallel} = (0, 0)$. The intensity of the ω_- mode is weaker with decreasing ω and vanishes at $\omega = 0$. An interesting feature is that the ω_- mode crosses the continuum

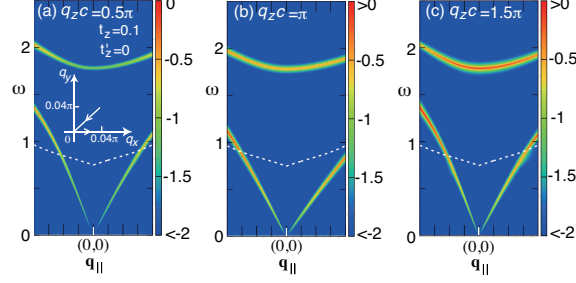


FIG. 4. Intensity maps of $\log_{10} |\text{Im}\kappa(\mathbf{q}, \omega)|$ in the vicinity of $\mathbf{q}_{||} = (0, 0)$ along $(0.04\pi, 0.04\pi)$ - $(0, 0)$ - $(0.04\pi, 0)$ [see the inset in (a)] for three choices of $q_z c$: (a) $q_z c = 0.5\pi$, (b) $q_z c = \pi$, and (c) $q_z c = 1.5\pi$. The ω_- mode is gapless at $\mathbf{q}_{||} = (0, 0)$ in spite of the presence of $t_z = 0.1$. The white dotted curve denotes the upper boundary of the particle-hole continuum. To keep an appropriate contrast, the same color is used below -2 and above 0.

smoothly without showing a clear structure and extends down to zero energy. A reason for that lies in very small spectral weight of the continuum around $\mathbf{q}_{||} = (0, 0)$. In fact, the difference of the spectral weight across the upper boundary of the continuum is not visible in the color scale in Fig. 4. On the other hand, the ω_+ mode has finite spectral weight at $\mathbf{q}_{||} = (0, 0)$ when $0 < q_z c < 2\pi$.

The right panels in Fig. 3 show maps of the denominator of $\text{Im}\kappa(\mathbf{q}, \omega)$ [Eq. (43)], more precisely the square of the modulus of Eq. (48) for a sequence of $q_z c$. The corresponding $\text{Im}\kappa(\mathbf{q}, \omega)$ shown in the left panels can have a peak along (approximately along) the minimum of the denominator of $\text{Im}\kappa(\mathbf{q}, \omega)$ above (below) the continuum. In Fig. 3(a'), it is interesting that we have two minima of the denominator for a given $\mathbf{q}_{||}$, but the finite spectral weight is realized only along the ω_+ mode and zero along a possible ω_- mode. At $q_z c = 2\pi$, on the other hand, both ω_+ and ω_- modes are realized along the minimum shown in Fig. 3(e') and have the finite spectral weight except for the ω_+ mode at $\mathbf{q}_{||} = (0, 0)$ in Fig. 3(e). In Fig. 3(d), the ω_+ mode has strong intensity only near $\mathbf{q}_{||} = (0, 0)$ and the intensity is suppressed as going away from $\mathbf{q}_{||} = (0, 0)$ although the denominator of Eq. (42) has a minimum there [Fig. 3(d')]. This is simply because of the $\mathbf{q}_{||}$ dependence of the numerator of Eq. (42). The ω_- mode is well visible even inside the continuum—below the white dotted curve in Figs. 3(b)–(d) and Figs. 4(a)–(c)—but the modulus of Eq. (48) gains additional values because of the mixture of the particle-hole excitations [Figs. 3(b')–(d')]. Therefore the peak position of the $\text{Im}\kappa(\mathbf{q}, \omega)$ deviates slightly from the minimum of Eq. (48) below

the white dotted curve in Figs. 3(b)–(d) and 4(a)–(c).

3. A smaller value of t_z

We have shown results at $t_z = 0.1$ and expect qualitatively similar results such as the vanishing of the ω_- mode at $q_z c = 0$ and the presence of the ω_{\pm} mode for $q_z c \neq 0$ for other choices of t_z . However, the spectral weight distribution may look different for a smaller t_z and it may be worth presenting those results, because several literature [53, 54] assumed $t_z = 0$ in the bilayer system, keeping the LRC among different layers.

Figures 5(a)–(e) are results at $t_z = 0.01$, which may be compared with Figs. 3(a)–(e). At $q_z c = 0$ [Fig. 5(a)], the only ω_+ mode is realized and quantitative changes are not visible even by employing a small t_z . However, at $q_z c = 0.5\pi$ [Fig. 5(b)], it might seem that only one mode is realized. In reality, the ω_+ mode has much larger spectral weight and the ω_- mode is hardly visible in the scale of Fig. 5(b). A sharp contrast to Fig. 3(b) is that the ω_+ mode suggests a gapless mode. However, it is not the case. The ω_+ mode acquires a small gap due to a small t_z whereas the ω_- mode is gapless similar to Fig. 3(b). These features are checked by magnifying a region around $\mathbf{q}_{\parallel} = (0, 0)$ as shown in Fig. 6(a).

At $q_z c = \pi$ [Fig. 5(c)], still only one mode seems to exist, but both ω_{\pm} modes do exist. A split is only visible by magnifying the vicinity around $\mathbf{q}_{\parallel} = (0, 0)$ as shown in Fig. 6(b) and the ω_+ mode seems to almost overlap with the ω_- mode in the other regions. This feature is typical for a small t_z at $q_z c = \pi$. From Eq. (45), we can check that $V_-(\mathbf{q}) = 0$ at $q_z c = \pi$. Equations (42) and (43) then imply that the plasmon dispersion is given by

$$[1 - \kappa_{\text{even}}^0(V(\mathbf{q}) + V_+(\mathbf{q}))][1 - \kappa_{\text{odd}}^0(V(\mathbf{q}) - V_+(\mathbf{q}))] = 0. \quad (62)$$

When t_z is small, we have $\kappa_{\text{even}}^0 \approx \kappa_{\text{odd}}^0$. Equation (45) indicates that $V_+(\mathbf{q}) \propto \tilde{h}_2 + \tilde{h}_4 \cos q_z c = \tilde{h}_2 - \tilde{h}_4 (> 0)$ at $q_z c = \pi$ for $0 < d < c/2$. This means that $V_+(\mathbf{q})$ has a minimum at $q_z c = \pi$ because \tilde{h}_2 and \tilde{h}_4 are positive. This analysis explains the reason why the ω_{\pm} modes become almost degenerate at $q_z c = \pi$. To see the splitting of these two modes at $q_z c = \pi$ more clearly even away from $\mathbf{q}_{\parallel} = (0, 0)$, the damping factor Γ should be taken smaller; see Appendix B.

At $q_z c = 1.5\pi$ [Fig. 5(d)], the ω_+ mode is well separated, although its spectral weight is relatively weak around $\mathbf{q}_{\parallel} = (0, 0)$. When we magnify such a region in Fig. 6(c), it is clearly

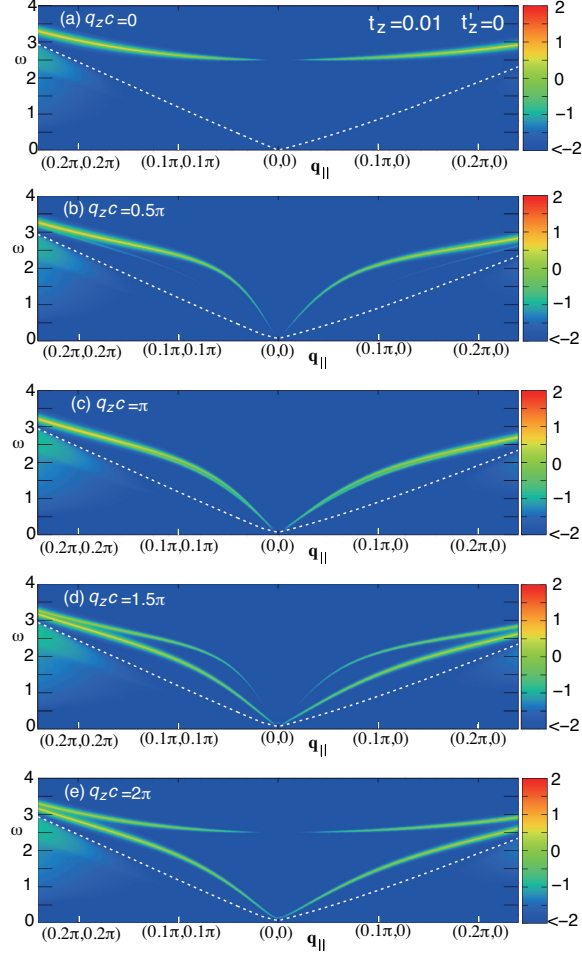


FIG. 5. Intensity map of $\log_{10} |\text{Im}\kappa(\mathbf{q}, \omega)|$ at $t_z = 0.01$ for a sequence of $q_z c$ around a region of $\mathbf{q}_{||} = (0, 0)$: (a) $q_z c = 0$, (b) $q_z c = 0.5\pi$, (c) $q_z c = \pi$, (d) $q_z c = 1.5\pi$, and (e) $q_z c = 2\pi$. The white dotted curve denotes the upper boundary of the particle-hole continuum. It becomes zero at $\mathbf{q}_{||} = (0, 0)$ and $q_z c = 0$ and finite for the other values of $q_z c$. To keep an appropriate contrast, the same color is used below -2.

visible that the ω_+ mode is acousticlike with a small gap at $\mathbf{q}_{||} = (0, 0)$ due to a small t_z whereas the ω_- mode is gapless.

At $q_z c = 2\pi$ [Fig. 5(e)], the ω_{\pm} modes are well separated—the ω_+ mode is opticallike and the ω_- mode is acousticlike with a small gap coming from a small t_z . This is in a sharp contrast to the cases for $q_z c \neq 2n\pi$ [Figs. 5(b)–(d) and 6(a)–(c)].

We have performed the same calculations at $t_z = 0$ and checked that results at $t_z = 0$ hardly change from those at $t_z = 0.01$ except that the ω_+ (ω_-) mode also becomes gapless at $q_z c \neq 2n\pi$ [$q_z c = 2n\pi (n \neq 0)$].

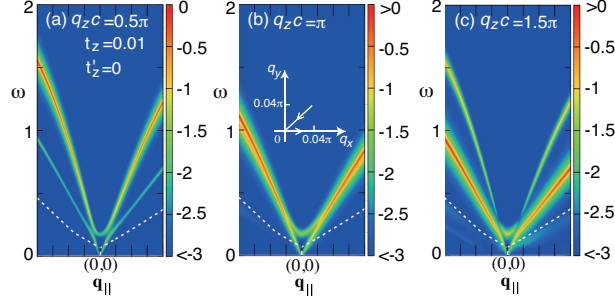


FIG. 6. Intensity maps of $\log_{10} |\text{Im}\kappa(\mathbf{q}, \omega)|$ in the vicinity of $\mathbf{q}_{||} = (0, 0)$ along $(0.04\pi, 0.04\pi)$ – $(0, 0)$ – $(0.04\pi, 0)$ [see the inset in (b)] for (a) $q_z c = 0.5\pi$, (b) $q_z c = \pi$, and (c) $q_z c = 1.5\pi$. The ω_+ mode acquires a small gap at $\mathbf{q}_{||} = (0, 0)$ due to the presence of a small $t_z = 0.01$. The white dotted curve denotes the upper boundary of the particle-hole continuum. To keep an appropriate contrast, the same color is used below -3 and above 0.

4. A large value of t_z

We also study a large value of t_z for completeness. Maps of the spectral function are shown in Fig. 7 for a sequence of $q_z c$. At $q_z c = 0$ [Fig. 7(a)], only one mode is realized as in the case of Figs. 3(a) and 5(a). The spectral intensity at $\mathbf{q}_{||} = (0, 0)$ is zero, indicating that it should be in-phase charge fluctuations between the two layers inside the unit cell because of the charge conservation. That is, it should be the ω_+ mode. At $q_z c = 0.5\pi$, there appear two modes as shown in Fig. 7(b). While this feature is the same as that in Fig. 3(b), the upper mode forms a convex shape around $\mathbf{q}_{||} = (0, 0)$ for $t_z = 0.25$ whereas the other mode is gapless as clarified in Fig. 8(a). A similar feature is observed for other $q_z c$ in Figs. 7(c)(d) and 8(b)(c). It is remarkable that this low-energy mode is sharply defined even inside the continuum. At $q_z c = 2\pi$ [Fig. 7(e)], there appear two gapped modes. In contrast to the case of $t_z = 0.1$ [Fig. 3(e)], it is the lower-energy mode that is similar to the mode at $q_z c = 0$ [Fig. 7(a)] and the spectral weight at $\mathbf{q}_{||} = (0, 0)$ vanishes. This indicates that the mode with lower energy should be the ω_+ mode. Because of the continuity of the mode as a function of $q_z c$ (see also Sec. III A 6), it is natural to conclude that the ω_+ mode becomes gapless in $q_z c \neq 2n\pi$ in Figs. 7(b)–(d) and 8(a)–(c) and the ω_- mode is always gapped independent of $q_z c$, except it vanishes at $q_z c = 0$ [Fig. 7(a)]. Therefore, it is implied that the energy hierarchy of the ω_{\pm} modes is interchanged for a large t_z .

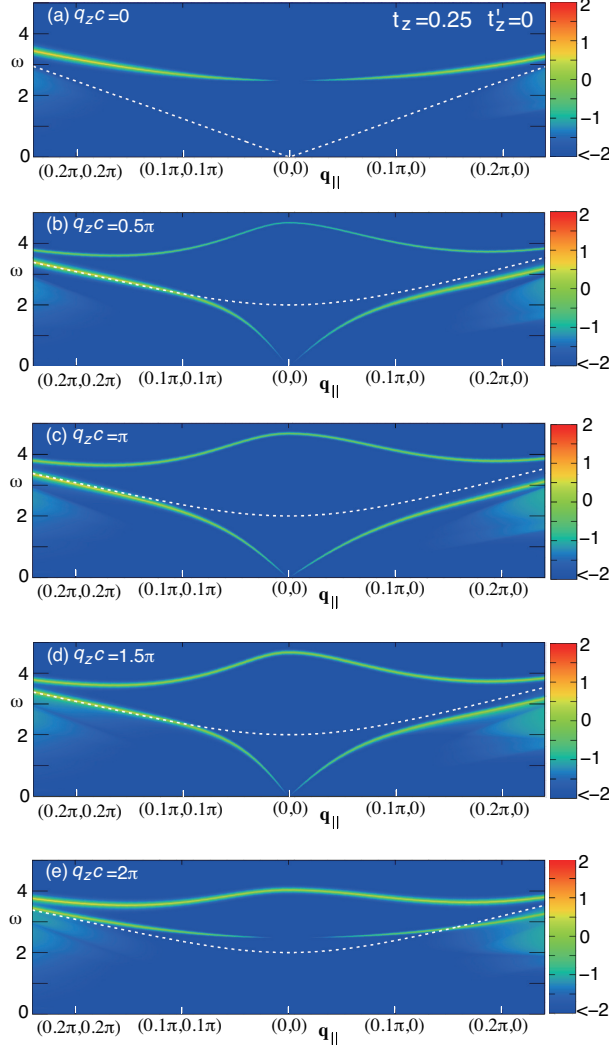


FIG. 7. Intensity maps of $\log_{10} |\text{Im}\kappa(\mathbf{q}, \omega)|$ for a sequence of $q_z c$ around a region of $\mathbf{q}_{\parallel} = (0, 0)$: (a) $q_z c = 0$, (b) $q_z c = 0.5\pi$, (c) $q_z c = \pi$, (d) $q_z c = 1.5\pi$, and (e) $q_z c = 2\pi$. The white dotted curve denotes the upper boundary of the particle-hole continuum. It becomes zero at $\mathbf{q}_{\parallel} = (0, 0)$ and $q_z c = 0$ even for a finite $t_z = 0.25$. To keep an appropriate contrast, the same color is used below -2.

5. t_z dependence of the gap at $\mathbf{q}_{\parallel} \approx (0, 0)$

The results for $t_z = 0.01, 0.1, 0.25$ (Figs. 3 – 8) imply that the gap of plasmon modes at $\mathbf{q}_{\parallel} \approx (0, 0)$ depends on t_z in a nontrivial way. We here clarify its t_z dependence.

Figure 9(a) is representative results for $q_z c = 2n\pi$ with n being integer—note that only the ω_+ mode is present at $q_z c = 0$, as already shown in Figs. 3(a), 5(a), and 7(a). Since

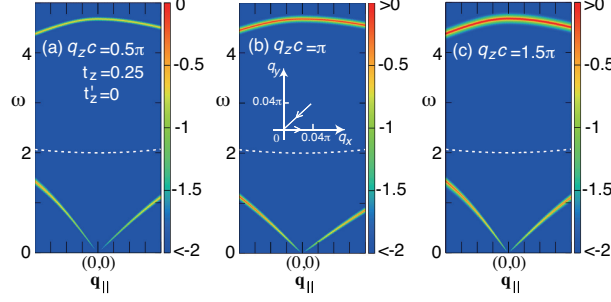


FIG. 8. Intensity maps of $\log_{10} |\text{Im}\kappa(\mathbf{q}, \omega)|$ in the vicinity of $\mathbf{q}_{||} = (0, 0)$ along $(0.04\pi, 0.04\pi)$ -($0, 0$)-($0.04\pi, 0$) [see the inset in (b)] for (a) $q_z c = 0.5\pi$, (b) $q_z c = \pi$, and (c) $q_z c = 1.5\pi$. It is the ω_+ mode that becomes gapless and the ω_- mode is gapped for a large t_z . The white dotted curve denotes the upper boundary of the particle-hole continuum. To keep an appropriate contrast, the same color is used below -2 and above 0.

the ω_{\pm} modes are realized above the particle-hole continuum, we plot the minimum position of Eq. (48) in Fig. 9(a) to achieve stable computation. The energy of the ω_+ mode is essentially independent of t_z whereas the energy of the ω_- mode increases monotonically with t_z . Interestingly for a large $t_z (\geq 0.16)$, the ω_- mode has energy higher than the ω_+ mode.

On the other hand, Fig. 9(b) is a representative result for $q_z c \neq 2n\pi$, showing very different behavior to that at $q_z c = 2n\pi$. The energy of the ω_+ mode increases monotonically with increasing t_z . Furthermore, the ω_+ mode follows perfectly the minimum position of Eq. (48) since it is always realized above the continuum. The energy of the ω_- mode is zero independent of t_z as already indicated in Figs. 4 and 6. Its energy is deviated from the minimum position of Eq. (48) as increasing t_z . This is because in contrast to the ω_+ mode, the ω_- mode is realized inside the particle-hole continuum as shown by the dashed line in Fig. 9(b), when $\mathbf{q}_{||}$ is close to $(0, 0)$. These descriptions hold up to $t_z \approx 0.15$. As seen in Fig. 9(a), the ω_+ mode becomes lower than the ω_- mode in $t_z \geq 0.16$ at $q_z c = 2n\pi$. Consequently, it is the ω_+ mode that exhibits a gapless mode and the ω_- mode is gapped in $t_z \geq 0.16$ for $q_z c \neq 2n\pi$. Therefore, by crossing $t_z \approx 0.16$, the energy hierarchy of the ω_{\pm} modes is interchanged as already implied in Fig. 7.

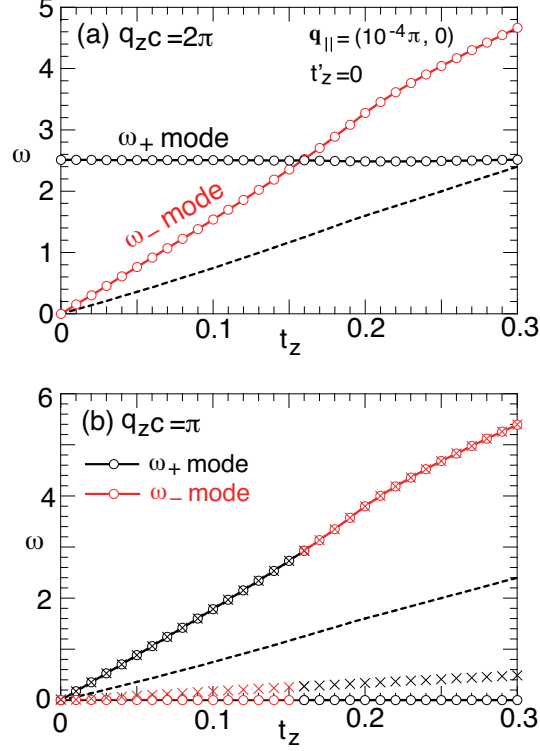


FIG. 9. t_z dependence of the gap of the ω_{\pm} modes at $\mathbf{q}_{\parallel} = (10^{-4}\pi, 0)$ for (a) $q_z c = 2\pi$ and (b) $q_z c = \pi$. The dashed line is the upper boundary of the continuum spectrum. In (a), the ω_{\pm} modes are determined from the minimum position of Eq. (48). The point $\omega_- = 0$ at $t_z = 0$ is introduced by hand for technical reasons. In (b), crosses denote the minimum positions of Eq. (48). They deviate from the ω_{\pm} -mode energy at low energy because of the mixture of the particle-hole continuum. Note that the energy of the ω_{\pm} modes is interchanged across $t_z \approx 0.16$ because of the crossing of these modes at $q_z c = 2n\pi$ as shown in (a).

6. $q_z c$ dependence

So far we have chosen certain points of $q_z c$. Here we clarify the $q_z c$ dependence of the ω_{\pm} modes. Figure 10(a) shows results at $\mathbf{q}_{\parallel} = (0.02\pi, 0)$ for $t_z = 0.1$. A white dotted line is the upper boundary of the particle-hole continuum. The ω_+ mode is always realized above the continuum. A peak at $q_z c = 2n\pi$ corresponds to the optical plasmon. The energy of the ω_+ mode is quickly decreased as going away from $q_z c = 2n\pi$ and becomes essentially $q_z c$ independent until the next peak at $q_z c = 2(n+1)\pi$. The ω_- mode does not exist at $q_z c = 0$, which is evident from the zero intensity there in Fig. 10(a). However, as going away

from $q_z c = 0$, the ω_- mode immediately gains the intensity and starts to show a dispersion between $\omega \approx 0.4$ – 1.6 with a peak at $q_z c = 2n\pi$ ($n \neq 0$). Interestingly this dispersive feature occurs crossing the upper boundary of the continuum.

Figure 10(b) is the same plot but for $\mathbf{q}_{\parallel} = (0.05\pi, 0)$. As we have seen in Fig. 4, the ω_+ mode has a weak \mathbf{q}_{\parallel} dependence around $\mathbf{q}_{\parallel} = (0, 0)$ and thus the result is similar to that in Fig. 10(a). On the other hand, the ω_- mode exhibits a cosinelike dispersion along the $q_z c$ direction and is located above the continuum.

In both Figs. 10(a) and (b), the intensity of the ω_{\pm} modes has a characteristic $q_z c$ dependence. In particular, the ω_+ mode loses intensity around $q_z c = 7\pi$ and both ω_{\pm} modes have a kind of “nodes” at specific $q_z c$ values. These positions depend on the choices of parameters (except for the vanishing intensity of the ω_- mode at $q_z c = 0$) and originate from the suppression of the numerator of $\text{Im}\kappa(\mathbf{q}, \omega)$ in Eq. (42). In other words, the absence of 2π periodicity in Fig. 10 originates from the numerator of Eq. (42), namely, the factor of $\cos^2 \frac{q_z d}{2}$,

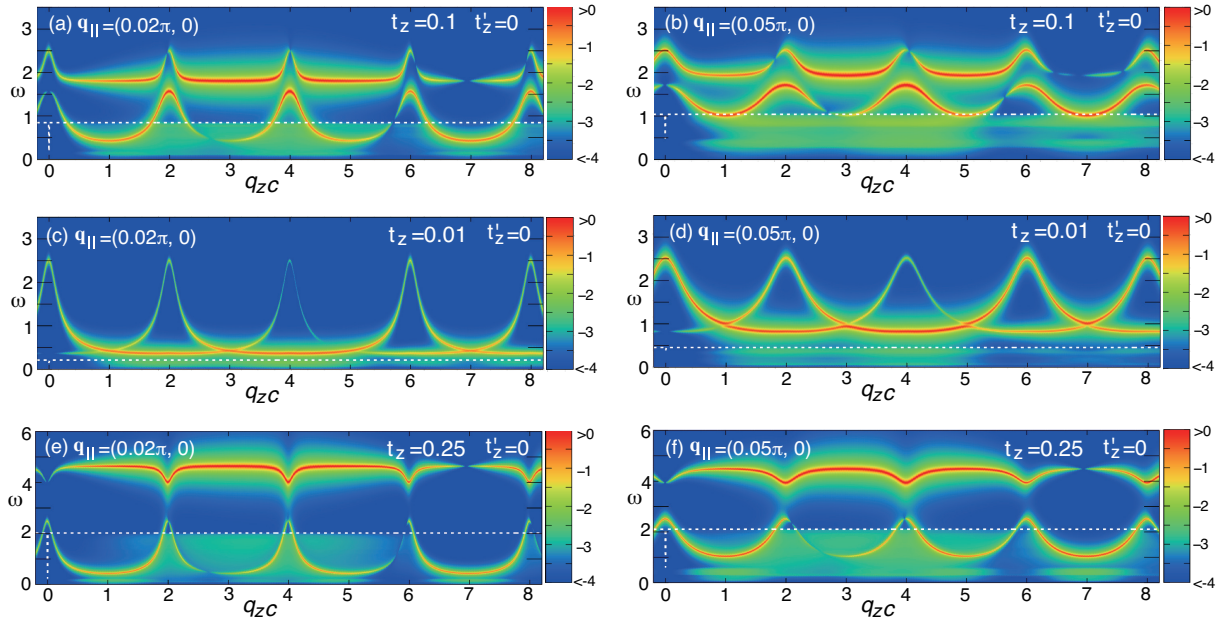


FIG. 10. $q_z c$ dependence of the intensity map of $\log_{10} |\text{Im}\kappa(\mathbf{q}, \omega)|$ at (a) $\mathbf{q}_{\parallel} = (0.02\pi, 0)$ and (b) $\mathbf{q}_{\parallel} = (0.05\pi, 0)$ for $t_z = 0.1$. The corresponding results of $t_z = 0.01$ and 0.25 are shown in (c)(d) and (e)(f), respectively. To get a reasonable contrast, the same color is used above 0 and below -4 . The white dotted line is the upper boundary of the continuum spectrum and exhibits a spike at $q_z c = 0$ because of the vanishing of the ω_- mode there.

$\sin^2 \frac{q_z d}{2}$, and $\frac{V'(\mathbf{q})+V'(-\mathbf{q})}{2}$. In fact, it is easily checked that the denominator of $\text{Im}\kappa(\mathbf{q}, \omega)$ [Eq. (43)], i.e., Eq. (48) retains 2π periodicity along the $q_z c$ direction; see Figs. 14(c) and (d).

The $q_z c$ dependence of the ω_{\pm} modes gives a different impression for a smaller t_z . We present corresponding results for $t_z = 0.01$ in Figs. 10(c) and (d). While the intensity of the ω_- mode vanishes at $q_z c = 0$ as we have already explained, the ω_- mode has a much weaker dispersion—almost flat—than that at $t_z = 0.1$. In particular, the ω_- mode does not exhibit a peak even at $q_z c = 2n\pi (n \neq 0)$, in a sharp contrast to the case of $t_z = 0.1$. That is, the ω_- mode tends to have a weaker dispersive feature with decreasing t_z . In contrast, the ω_+ mode has a much stronger dispersion between $\omega \approx 0.5$ – 2.5 in Fig. 10(c) and $\omega \approx 1$ – 2.5 in Fig. 10(d), compared with that for $t_z = 0.1$ shown in Figs. 10(a) and (b), respectively, even though t_z is much smaller. As we have already seen in Figs. 5(c) and 6(b), the ω_{\pm} modes almost overlap with each other at $q_z c = \pi + 2n\pi$.

For a large t_z , as we have shown in Fig. 9, the ω_- mode has higher energy than the ω_+ mode. This can also be confirmed by zero spectral weight at $q_z c = 0$ in the higher-energy mode in Figs. 10(e)(f)—a characteristic feature of the ω_- mode as we have already discussed in the context of Fig. 3(a). The ω_- mode shows the $q_z c$ dependence very different from Figs. 10(a)–(d): the ω_- mode has a dip at $q_z c = 2n\pi$, not a peak there, in Figs. 10(e)(f), and an almost flat feature away from $q_z c = 2n\pi$. In particular, the dip of the ω_- mode touches with a peak of the ω_+ mode at $q_z c = 2n\pi$ at $t_z \approx 0.16$, where the energy of the ω_{\pm} mode is interchanged. In contrast to the ω_- mode, the lower-energy mode, namely ω_+ mode, has a large dispersive feature at $\mathbf{q}_{\parallel} = (0.02\pi, 0)$ between $\omega \approx 0.5$ – 2.5 and is sharply defined even though the ω_+ mode is realized inside the continuum especially for $q_z c \neq 2n\pi$. This is simply due to low spectral weight of the continuum especially around $\mathbf{q}_{\parallel} = (0, 0)$. At $\mathbf{q}_{\parallel} = (0.05\pi, 0)$ shown in Fig. 10(f), the ω_+ mode is similar to that at $\mathbf{q}_{\parallel} = (0.02\pi, 0)$ [Fig. 10(e)], but becomes less dispersive.

One would expect a larger $q_z c$ dispersion for a larger t_z because the system is closer to be three dimensional. However, Figs. 10(a)(c)(e) do not support such a native expectation. The ω_+ mode has a large dispersion in $0.5 \lesssim \omega \lesssim 2.5$ at $t_z = 0.01$ and 0.25 , but a smaller dispersion in $2 \lesssim \omega \lesssim 2.5$ at $t_z = 0.1$. The ω_- mode, on the other hand, it is almost dispersionless at $t_z = 0.01$ and has a larger dispersion in $0.5 \lesssim \omega \lesssim 1.5$ at $t_z = 0.1$, but an almost flat dispersion in $4 \lesssim \omega \lesssim 4.5$ at $t_z = 0.25$.

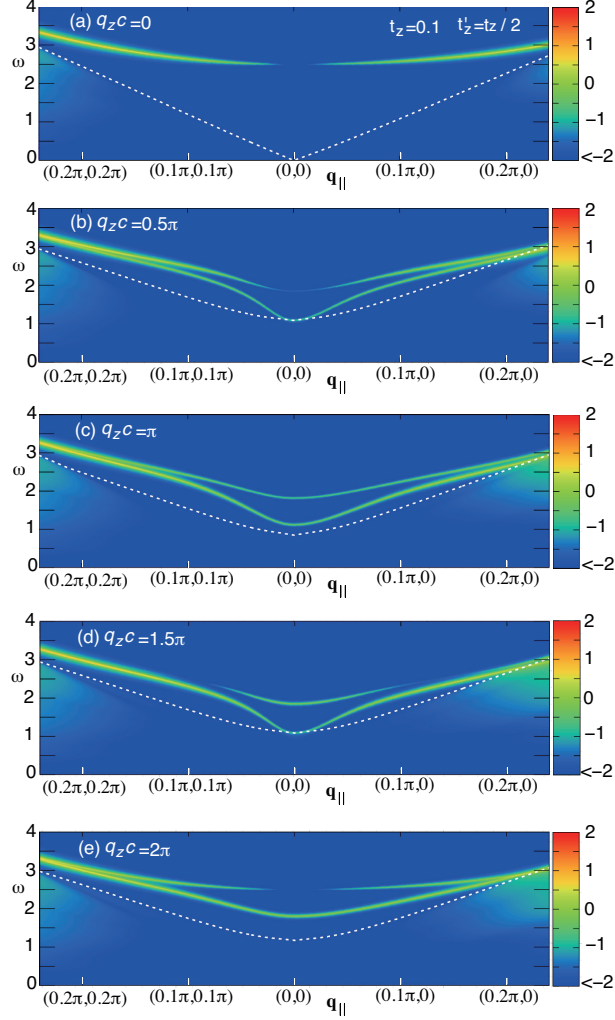


FIG. 11. Intensity map of $\log_{10} |\text{Im}\kappa(\mathbf{q}, \omega)|$ for a sequence of $q_z c$ around a region of $\mathbf{q}_{||} = (0, 0)$: (a) $q_z c = 0$, (b) $q_z c = 0.5\pi$, (c) $q_z c = \pi$, (d) $q_z c = 1.5\pi$, and (e) $q_z c = 2\pi$. The interbilayer hopping t'_z is introduced as $t'_z = t_z/2 = 0.05$. The white dotted curve denotes the upper boundary of the particle-hole continuum. There is no continuum spectrum at $\mathbf{q}_{||} = (0, 0)$ and $q_z c = 0$ even for a finite $t_z = 0.1$ and $t'_z = 0.05$. To keep an appropriate contrast, the same color is used below -2.

B. Charge excitation spectra with $t'_z \neq 0$

So far we have focused on the case of $t'_z = 0$, no interbilayer hopping, although electrons in all layers interact with each other via the LRC. Here we first focus on the case of $t_z = 0.1$ and study the effect of t'_z by assuming $t'_z = t_z/2$. Since results may become different for a large t_z as seen in Figs. 7 and 8, such results shall be presented in the last section 4.

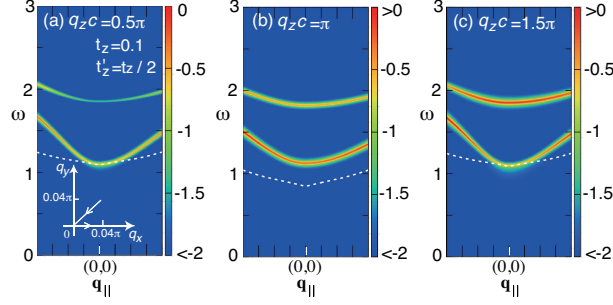


FIG. 12. Intensity maps of $\log_{10} |\text{Im}\kappa(\mathbf{q}, \omega)|$ in the vicinity of $\mathbf{q}_{||} = (0, 0)$ along $(0.04\pi, 0.04\pi)$ -($0, 0$)-($0.04\pi, 0$) [see the inset in (a)] for various choices of $q_z c$: (a) $q_z c = 0.5\pi$, (b) $q_z c = \pi$, and (c) $q_z c = 1.5\pi$. The interbilayer hopping t'_z is introduced as $t'_z = t_z/2 = 0.05$. The white dotted curve denotes the upper boundary of the particle-hole continuum. To keep an appropriate contrast, the same color is used above 0 and below -2.

1. Maps of the spectral weight

Results corresponding to Figs. 3(a)–(e) are shown in Figs. 11(a)–(e) in the same condition except for a finite $t'_z = t_z/2 = 0.05$. At $q_z c = 0$ [Fig. 11(a)], only the ω_+ mode is realized and the spectrum is essentially the same as Fig. 3(a), that is, the effect of t'_z is negligible at $q_z c = 0$. In fact, mathematically one can check that we obtain the same expression as Eq. (61) at $q_z c = 0$. The negligible effect of t'_z also applies to the result at $q_z c = 2\pi$ [Fig. 11(e)], except that the ω_- mode has a slightly larger energy because of the inclusion of t'_z . The major effect of t'_z is recognized at $q_z c \neq 2n\pi$. Whereas the ω_+ mode exhibits a dispersion very similar to Figs. 3(b)–(d), the ω_- mode is gapped at $\mathbf{q}_{||} = (0, 0)$ by a finite t'_z . Consequently we obtain two gapped modes at any $q_z c (\neq 0)$.

To emphasize this qualitative change, we also show the zoom of the spectrum around $\mathbf{q}_{||} = (0, 0)$ in Figs. 12(a)–(c). These results clearly demonstrate that the spectrum of the ω_- mode becomes gapped by including t'_z especially in the vicinity of $\mathbf{q}_{||} = (0, 0)$, in sharp contrast to Figs. 4(a)–(c).

2. t_z dependence of the gap at $\mathbf{q}_{||} \approx (0, 0)$

Next we clarify how the gap of the ω_{\pm} modes at $\mathbf{q}_{||} = (0, 0)$ evolves with t_z and $t'_z (= t_z/2)$. Figure 13(a) shows a representative result at $q_z c = 2n\pi$ although the ω_- mode vanishes at

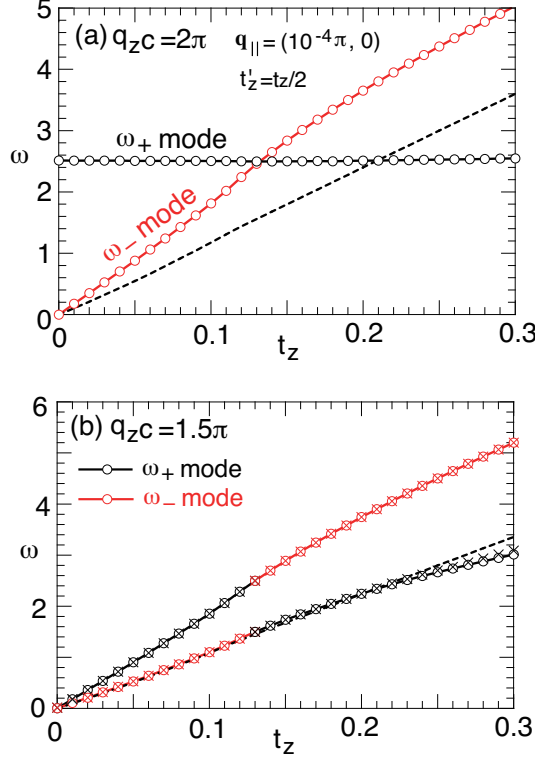


FIG. 13. t_z dependence of the gap of the ω_{\pm} modes at $\mathbf{q}_{\parallel} = (10^{-4}\pi, 0)$ at (a) $q_z c = 2\pi$ and (b) $q_z c = 1.5\pi$. The dashed line is the upper boundary of the continuum spectrum. In (a), the ω_{\pm} modes are determined from the minimum position of Eq. (48). Since the ω_+ mode is located below the continuum in $t_z \gtrsim 0.2$, these energies are estimated approximately. The point $\omega_- = 0$ at $t_z = 0$ is introduced by hand for technical reasons. In (b), crosses denote the minimum position of Eq. (48); only one minimum position is found at $t_z = 0.01$.

$q_z c = 0$. Here, the gap energy of the ω_{\pm} modes is calculated from the minimum position of Eq. (48) to achieve stable computation. This is justified because the ω_{\pm} modes are realized above the continuum at least up to $t_z = 0.2$. In $t_z > 0.2$, the actual energy of the ω_+ mode may slightly deviate from the result in Fig. 13(a). The t_z dependence of the ω_+ mode can be negligible even in the presence of t'_z and the result is essentially the same as Fig. 9(a). The ω_- mode also exhibits a similar t_z dependence to Fig. 9(a) and the effect of t'_z is not crucial at $q_z c = 2n\pi$.

However, the presence of t'_z has a big effect for $q_z c \neq 2n\pi$ and the gapless mode disappears upon a finite t_z and $t'_z = t_z/2$, in sharp contrast to Fig. 9(b). Figure 13(b) shows results at $q_z c = 1.5\pi$. Both ω_{\pm} modes have higher energy with increasing t_z . A comparison with

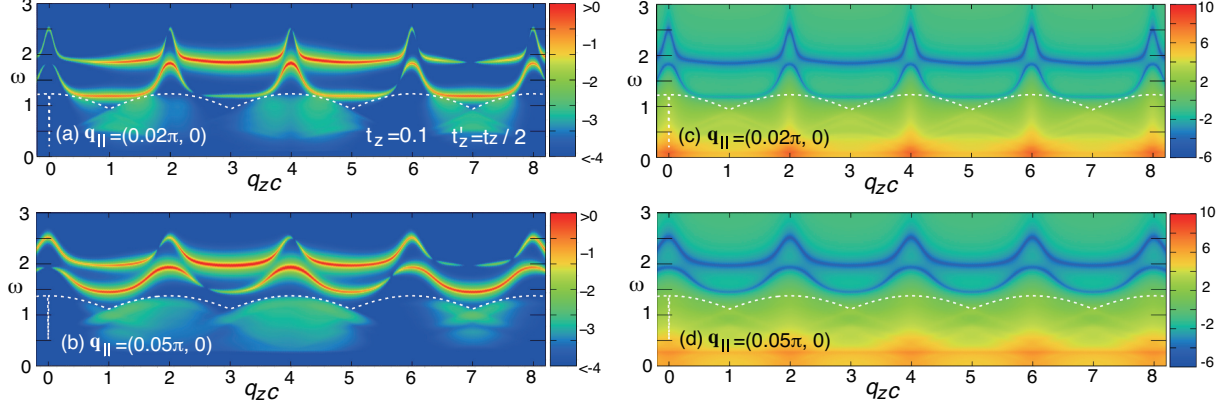


FIG. 14. $q_z c$ dependence of the intensity map of $\log_{10} |\text{Im}\kappa(\mathbf{q}, \omega)|$ (left panels) and $\log_{10} |\det|^2$ given in Eq. (50) (right panels) at $\mathbf{q}_{\parallel} = (0.02\pi, 0)$ (a) and (c), and $\mathbf{q}_{\parallel} = (0.05\pi, 0)$ (b) and (d) for $t'_z = t_z/2 = 0.05$. To get a reasonable contrast, the same color is used above 0 and below -4 in the left panels. The white dotted curve is the upper boundary of the continuum spectrum and exhibits a spike at $q_z c = 0$ where the ω_- mode vanishes.

Fig. 9(b) confirms that the gap of the ω_- (ω_+) mode in $t_z \leq 0.13$ (≥ 0.13) originates from a finite t'_z .

In Fig. 13(b), the energy of the ω_- mode is located close to the upper boundary of the particle-hole continuum in $t_z \leq 0.13$. In $t_z \geq 0.13$, however, the ω_+ mode has lower energy than the ω_- mode and is located close to the upper boundary of the continuum. In both regions, their energy position is well captured by the minimum position of Eq. (48) shown by crosses. If we choose $q_z c = \pi$ and would make the same plot as Fig. 13(b), the plasmon modes would be realized above the continuum even for a large t_z , which may be readily inferred from Figs. 11(c) and 12(b).

3. $q_z c$ dependence

The $q_z c$ dependence of the ω_{\pm} modes is shown in Figs. 14(a) and (b) at $\mathbf{q}_{\parallel} = (0.02\pi, 0)$ and $(0.05\pi, 0)$, respectively. By comparing with Figs. 10(a)(b), essentially the same results are obtained except that the energy of the ω_- mode is pushed up to higher energy by a finite t'_z . While the intensity of the spectrum does not have 2π periodicity as discussed already in the context of Fig. 10, it is interesting that the spectrum is strongly suppressed at almost the same positions of $q_z c$ shown in Figs. 10(a)(b). That is, the effect of t'_z is weak for the

intensity dependence of the ω_{\pm} modes.

We can check analytically that the denominator of $\kappa(\mathbf{q}, \omega)$ in Eq. (49), i.e., Eq. (48) has 2π periodicity with respect to $q_z c$ and we show such a property in the right panels in Fig. 14, where its square of the modulus is presented. Therefore, the non- 2π periodicity of the intensity of the $\text{Im}\kappa(\mathbf{q}, \omega)$ originates from the numerator, namely, κ_{\cos}^0 and $V'_+(\mathbf{q})$ in Eq. (49).

4. Spectra for a large t_z

As we have seen in Sec. III A, the energy hierarchy of the ω_{\pm} modes is interchanged for a large t_z . This also happens in the presence of t'_z as already shown in Fig. 13. The presence of t'_z reduces the crossing value of t_z down to $t_z = 0.13$ when $t'_z = t_z/2$. This value of t_z may not be regarded so large and can be realistic for some bilayer materials. Hence, it should be useful to present how the spectrum looks like for a large t_z . To get a clear separation between the ω_{\pm} modes, we here choose $t_z = 0.25$.

\mathbf{q} - ω maps are shown in Figs. 15(a)–(e) for a sequence of $q_z c$. At $q_z c = 0$ [Fig. 15(a)], we have only the ω_+ mode and the spectral weight at $\mathbf{q}_{\parallel} = (0, 0)$ vanishes due to the charge conservation as we already explained in Sec. III A 2; the upper boundary of the particle-hole excitations is zero at $\mathbf{q}_{\parallel} = (0, 0)$. With increasing $q_z c$, the particle-hole continuum gains the spectral weight even at $\mathbf{q}_{\parallel} = (0, 0)$ and the ω_+ mode is realized just below its boundary. The ω_- mode has higher energy than the ω_+ mode and is located above the continuum. However, the proximity to $q_z c = 0$ yields tiny spectral weight and the ω_- mode is barely visible with a convex upward centered at $\mathbf{q}_{\parallel} = (0, 0)$ and $\omega \approx 4.5$ in Fig. 15(b). This ω_- mode becomes more visible with increasing $q_z c$ as shown in Figs. 15(c)(d)(e) with a small $q_z c$ dependence. The ω_+ mode has energy lower than the ω_- mode and is realized just above the continuum spectrum at $q_z c = \pi$ [Fig. 15(c)], but enters into the continuum for larger $q_z c$ as seen in Figs. 15(d)(e). The reason why the ω_+ mode is relatively sharp even inside the continuum lies in small spectral weight of the continuum around $\mathbf{q}_{\parallel} = (0, 0)$: it tends to be broadened around $\mathbf{q}_{\parallel} = (0.2\pi, 0.2\pi)$ and $(0.2\pi, 0)$, sufficiently away from $(0, 0)$.

In Fig. 15(f), we present the $q_z c$ dependence of the spectral intensity at $\mathbf{q}_{\parallel} = (0.02\pi, 0)$. It is interesting that both ω_{\pm} modes have a smaller dispersion in spite of a large t_z and the system becomes more three dimensional by comparing with Fig. 14. The ω_+ mode is sharply

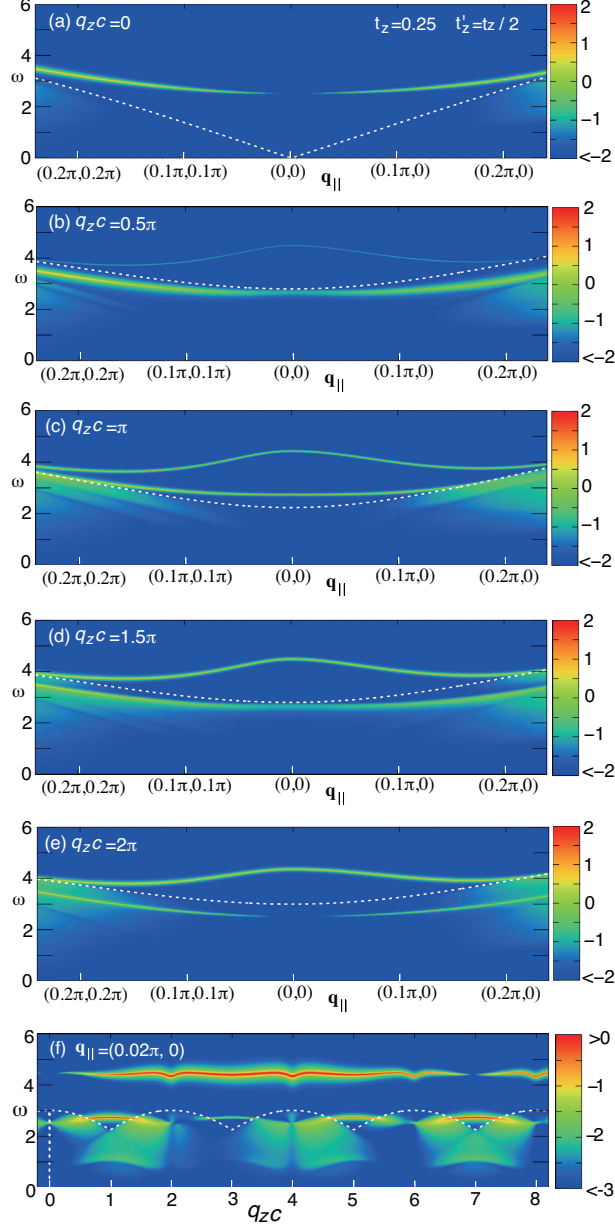


FIG. 15. Intensity map of $\log_{10} |\text{Im} \kappa(\mathbf{q}, \omega)|$ in the presence of a large $t_z = 0.25$ and $t'_z = t_z/2$. (a)–(e) \mathbf{q}_{\parallel} dependence for a sequence of $q_z c$ around a region of $\mathbf{q}_{\parallel} = (0, 0)$: (a) $q_z c = 0$, (b) $q_z c = 0.5\pi$, (c) $q_z c = \pi$, (d) $q_z c = 1.5\pi$, and (e) $q_z c = 2\pi$. (f) $q_z c$ dependence of the intensity map of $\log_{10} |\text{Im} \kappa(\mathbf{q}, \omega)|$ at $\mathbf{q}_{\parallel} = (0.02\pi, 0)$. The white dotted curve denotes the upper boundary of the particle-hole continuum—there is no continuum spectrum at $\mathbf{q}_{\parallel} = (0, 0)$ and $q_z c = 0$ even for a finite t_z and t'_z in (a) and there is a spike at $q_z c = 0$ in (f) because of the disappearance of the ω_- mode there. To keep an appropriate contrast, the same color is used below -2 in (a)–(e), and above 0 and below -3 in (f).

defined above the continuum around $q_z c = \pi + 2n\pi$ although its intensity depends on $q_z c$. Around $q_z c = 2n\pi$, on the other hand, the ω_+ mode is blurred substantially by the mixture of the continuum spectrum. The ω_+ mode can be traced better in Figs. 15(a)–(e) rather than the $q_z c$ dependence in Fig. 15(f). The ω_- mode vanishes at $q_z c = 0$ and exhibits an almost flat dispersion as a function of $q_z c$ in Fig. 15(f). In particular, as seen in Figs. 10(e)(f), the ω_- mode exhibits a dip at $q_z c = 2n\pi (n \neq 0)$. The ω_- mode is hardly visible at $q_z c = 7\pi$, which is due to the band parameters, especially a specific value of d/c , and has been already observed in Figs. 10(e)(f).

IV. DISCUSSION

A. Comparison with RIXS data

We are aware of RIXS data of plasmon excitations in Y-based cuprates [52]. These data were analyzed by employing the LRC obtained in the electron-gas model [53, 54]. Although such an analysis may not be justified in a strict sense for a system near half-filling such as in cuprates (electron-liquid systems), the authors expected to clarify whether the experimental data may be related to the q^{-2} singularity of the LRC, the essential feature to realize plasmon excitations, namely, a physics of the long-wavelength limit.

The present theory extends the Fetter model [53, 54] by deriving the LRC [Eqs. (28) and (29)] in the bilayer lattice structure and making it applicable to any electron density. Hence it is interesting to confirm that the experimental data are indeed interpreted as plasmon excitations. We can find a parameter set to reproduce the experimental data as shown in Fig. 16 when we choose $t = 233$ meV. This value is smaller than the value obtained in *ab initio* calculations [64, 67, 68]. Our t should be interpreted as an effective one and thus becomes smaller than the bare value, especially when making a comparison with experimental data [48]. Our results partly share those given in Ref. [52], but important differences are revealed.

At $q_z c = 1.8\pi$, the ω_- mode has higher intensity than the ω_+ mode and the experimental data follow the ω_- mode. The same conclusion was obtained by studying the coupling to the superconducting phase to the electromagnetic fields [69]. In Ref. [52], $q_z c = 0.2\pi$ was considered by assuming 2π periodicity with respect to $q_z c$ and it was concluded that the ω_+ mode followed the experimental data. However, as we have shown explicitly in Fig. 10, the

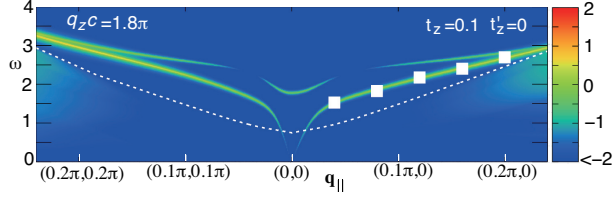


FIG. 16. Comparison with the plasmon energy (solid squares) reported in Y-based cuprate superconductors in Ref. [52]; t is assumed to be 233 meV. The experimental data are superimposed on the intensity map of $\log_{10} |\text{Im}\kappa(\mathbf{q}, \omega)|$ at $q_z c = 1.8\pi$, $t_z = 0.1$, and $t'_z = 0$. The white dotted curve denotes the upper boundary of the particle-hole continuum. To keep an appropriate contrast, the same color is used below -2.

plasmon intensity can have a strong $q_z c$ dependence. In particular, as we have emphasized in the context of Figs. 3(a) and (e), $q_z c = 0$ is a special point and the ω_- mode disappears there, but not $q_z c = 2n\pi (n \neq 0)$. The modulation of the peak intensity originates from the numerator of Eq. (42) via the factor $q_z d$, namely the geometry of the lattice structure. Nonetheless, we cannot deny a possibility that we could find another parameter set which allows the experimental data to be interpreted as the ω_+ mode. In addition, one should be careful because the energy hierarchy of the ω_{\pm} modes is interchanged for $t_z \geq 0.16$ (0.13 for $t'_z = t_z/2$). To clarify which mode the RIXS data indicate, ω_+ mode or ω_- mode, further RIXS experiments are definitely necessary.

A practical procedure to identify the ω_{\pm} mode in RIXS measurements would be the following. Choose $q_z c = 2n\pi (n \neq 0)$ and $\mathbf{q}_{||} \approx (0, 0)$. When RIXS detects collective charge excitations, they should be related with the ω_- mode since the spectral weight of the ω_+ mode is expected to be negligible there [see Figs. 3(e) and 11(e)]. After that, $q_z c$ will be moved away from $2n\pi (n \neq 0)$ so that RIXS can trace the ω_- mode. At the same time, some additional signal is expected above or below the ω_- mode, depending on a value of t_z , which should be associated with the ω_+ mode.

To pursue a quantitative comparison with experiments, strong correlation effects should also be considered especially for cuprates and the obtained LRC on the bilayer lattice [Eqs. (28) and (29)] should be incorporated into the framework of the so-called t - J - V model [36], which is under way.

B. Comparison with the Fetter model

The Fetter model [53] was employed in Ref. [54] to study plasmon excitations in bilayer cuprates. Since $t_z = 0$ was taken in Ref. [54], we may compare our results at $t_z = 0.01$, which shows nearly the same results as those at $t_z = 0$.

In Ref. [54], they can take the limit of $d \rightarrow 0$, yielding $V(\mathbf{q}) = V'(\mathbf{q})$. This is a specific property of the electron-gas model and the electron density becomes double in this limit. In the present theory, however, the model is defined in $0 < d \leq c/2$. Although one can invoke a small d , the limit of $d = 0$ is not defined; instead, one should use a single-layer lattice model for $d = 0$, not the present model.

In Ref. [54], there is no 2π periodicity along the q_x and q_y directions whereas the present theory describes such 2π periodicity as it should do in crystals. In contrast, the periodicity was assumed along the q_z direction in Ref. [54] and the value of q_z is restricted in the first Brillouin zone. However, because of the multiple-point basis inside the unit cell along the z direction, the spectral weight of charge excitations, i.e., $\text{Im}\kappa(\mathbf{q}, \omega)$ does not have 2π periodicity along the q_z direction in the present model. A remarkable feature is that the denominator of the charge response function [Eqs. (43), (48), and (50)] retains 2π periodicity along the $q_z c$ direction even with a finite t'_z (see Fig. 14). This 2π periodicity is also present in Ref. [54].

In the limit of $\mathbf{q} \rightarrow \mathbf{0}$, Ref. [54] yields

$$V(\mathbf{q}) = V'(\mathbf{q}) \propto \frac{1}{(q_x c)^2 + (q_y c)^2 + (q_z c)^2}, \quad (63)$$

namely, an isotropic Coulomb interaction. Note that the lattice constant c appears behind q_x and q_y in their formalism. Instead, we obtain

$$V(\mathbf{q}) = V'(\mathbf{q}) \propto \frac{1}{\alpha [(q_x a)^2 + (q_y a)^2] + (q_z c)^2}, \quad (64)$$

respecting the lattice anisotropy even in the limit of $\mathbf{q} \rightarrow \mathbf{0}$.

The ω_- mode was discussed to show essentially no q_z dependence in Ref. [54]. We have obtained similar results when t_z is small; see Figs. 10(c) and (d). However, as we have shown in Figs. 10 and 14, the ω_- mode exhibits a sizable q_z dependence once a moderate t_z is introduced; in particular, the ω_- mode has a peak at $q_z c = 2n\pi$.

C. Short-range interaction without t'_z

Although we have considered the LRC, Eqs. (10) and (31) are valid for any functional form of $V(\mathbf{q})$ and $V'(\mathbf{q})$. It may be informative to consider a short-range Coulomb interaction such as

$$V(\mathbf{q}) = 2V_{xy}(\cos q_x + \cos q_y), \quad (65)$$

$$V'(\mathbf{q}) = V_z e^{-iq_z d}. \quad (66)$$

We may assume no interbilayer interaction. The resulting susceptibility has then the same structure as that in the non-interaction case:

$$\kappa(\mathbf{q}, \omega) = \cos^2 \frac{q_z d}{2} \kappa_{\text{even}}(\mathbf{q}, \omega) + \sin^2 \frac{q_z d}{2} \kappa_{\text{odd}}(\mathbf{q}, \omega), \quad (67)$$

where

$$\kappa_{\text{even}}(\mathbf{q}, \omega) = \frac{\kappa_{\text{even}}^0(\mathbf{q}, \omega)}{1 - (V(\mathbf{q}) + V_z) \kappa_{\text{even}}^0(\mathbf{q}, \omega)}, \quad (68)$$

$$\kappa_{\text{odd}}(\mathbf{q}, \omega) = \frac{\kappa_{\text{odd}}^0(\mathbf{q}, \omega)}{1 - (V(\mathbf{q}) - V_z) \kappa_{\text{odd}}^0(\mathbf{q}, \omega)}. \quad (69)$$

It is straightforward to do similar calculations for short-range magnetic interactions such as $J(\mathbf{q}) = 2J(\cos q_x + \cos q_y)$ and $J'(\mathbf{q}) = J_z e^{-iq_z d}$, yielding the dynamical magnetic susceptibility with the same functional forms as Eqs. (67), (68), and (69). This describes the so-called bilayer modulation, which was actually observed by inelastic neutron scattering experiments for Y-based cuprates [70, 71].

D. Charge ordering tendencies in cuprates

As mentioned in the Introduction, besides plasmons, charge ordering tendencies [8–19] including the spin-charge stripe order [6, 7] were observed in cuprate superconductors. The present comprehensive analysis with the long-range Coulomb interaction cannot capture those ordering tendencies. This suggests at least two possibilities. One is that those phenomena are driven by higher-order electron correlations beyond the RPA. The other is that those are not usual charge excitations that we have studied here, but related to bond-charge excitations whose energy scale is controlled by the spin exchange interaction J [72, 73],

indicating that the short-range magnetic interaction is also important. This idea indeed explained the data in electron-doped cuprates [20–22], but not in hole-doped cuprates [26–33]. A possible reason may lie in a fact that the charge ordering tendency was observed inside the pseudogap phase in the hole-doped cuprates and the effect of the pseudogap should have been considered more seriously.

V. CONCLUSIONS

We have performed a comprehensive study of charge excitations in a bilayer system with the LRC and obtain important formulae and insights beyond the existing knowledge. There are two major results in the present work.

The first one is a derivation of the LRC that fully respects the bilayer lattice structure and can be applicable to any electron density [Eqs. (28) and (29)]. This is an extension of the Fetter model formulated 50 years ago [53] and the differences to the outcome from the Fetter model are clarified in Sec. IV B. We also provide a general formula of the charge susceptibility for the LRC [Eq. (49)] and compare it with a short-range Coulomb-interaction case (see Sec. IV C). While we have discussed the data of Y-based cuprates in Sec. IV A, the present theory is general and can be applicable to other bilayer materials.

The second one is to elucidate numerically the charge excitation spectrum for the bilayer system where the LRC is dominant; see Sec. III. The spectral weight of plasmon dispersion loses 2π periodicity along the $q_z c$ direction. However, it is remarkable to find that Eq. (48) retains 2π periodicity even in the presence of the bilayer structure; we may indicate that a *fictitious* plasmon dispersion, not the spectral weight, has 2π periodicity in the $q_z c$ direction. As already pointed out in Ref. [54], the bilayer system hosts two modes: ω_+ and ω_- mode. Although electrons in each layer interact with each other via the LRC, we may turn off the interbilayer hopping t'_z approximately for some materials. When t_z is small, the ω_+ mode has higher energy than the ω_- mode and is gapped whereas the ω_- mode is gapped only at $q_z c = 2n\pi (n \neq 0)$ and exhibits a gapless mode for $q_z c \neq 2n\pi$ at $\mathbf{q}_{\parallel} = (0, 0)$. Interestingly when t_z becomes moderately large, the situation becomes vice versa: the ω_- mode has higher energy than the ω_+ mode and is gapped whereas the ω_+ mode is gapless for $q_z c \neq 2n\pi$ and gapped at $q_z c = 2n\pi$. The inclusion of t'_z yields a gap in both ω_{\pm} modes for $q_z c \neq 2n\pi$ whereas the modes at $q_z c = 2n\pi$ are hardly affected by t'_z . An unexpected

feature is that when the system becomes more three dimensional by introducing a larger t_z , the $q_z c$ dispersion of the modes is not necessarily enhanced.

The determination of the mode observed by RIXS is not straightforward. While we have found a parameter set that the recent RIXS data for Y-based cuprates [52] can be well explained by the ω_- mode, we cannot eliminate a possibility that other parameter sets could explain the data in terms of the ω_+ mode. More detailed analyses are necessary both theoretically and experimentally to determine the mode observed in RIXS [52], including a role of strong correlation effects beyond the present RPA. There is a subtlety that the energy hierarchy of the ω_{\pm} modes is interchanged by a moderately large, yet not unrealistic value of t_z . We have therefore proposed an idea to distinguish the ω_{\pm} modes in RIXS in Sec. IV A.

ACKNOWLEDGMENTS

The author thanks P. Jakubczyk, G. Khaliullin, W. Metzner, and M. Nieszporski for valuable discussions about how to formulate the LRC for the bilayer system, and M. Bejas and A. Fujimori for insightful discussions about plasmons in a bilayer system, and A. Greco and M. Hepting for constructive comments about the manuscript. The author is indebted to warm hospitality of Max-Planck-Institute for Solid State Research. He was supported by JSPS KAKENHI Grant No. JP20H01856 and World Premier International Research Center Initiative (WPI), MEXT, Japan.

Appendix A: Limit of $d \rightarrow c/2$

The general expression of Eqs. (28), (29), and $\kappa(\mathbf{q}, \omega)$ in Eq. (49) should be reduced to simpler expressions in the limit of $d \rightarrow c/2$. This may be a stringent test of the formalism given in the main text and thus we shall demonstrate that.

In the case of $c = 2d$ as well as $t_z = t'_z$, we obtain in Eq. (54)

$$\varphi_{\mathbf{k}\mathbf{k}+\mathbf{q}} = \begin{cases} 0 & \text{for } \cos(k_z d + q_z d) \geq 0 \\ \pi & \text{for } \cos(k_z d + q_z d) < 0 \end{cases} \quad (\text{A1})$$

which lead to $\kappa_{\sin}^0 = 0$ in Eq. (53). We then obtain the following simple expression:

$$\kappa_{11}^0 + \kappa_{\cos}^0 = \frac{2}{N} \sum_{\mathbf{k}} \frac{f(\lambda_{\mathbf{k}}^{c2d}) - f(\lambda_{\mathbf{k}+\mathbf{q}}^{c2d})}{\lambda_{\mathbf{k}}^{c2d} + \omega - \lambda_{\mathbf{k}+\mathbf{q}}^{c2d} + i\Gamma}, \quad (\text{A2})$$

and

$$\lambda_{\mathbf{k}}^{c2d} = \xi_{\mathbf{k}} - 2t_z(\cos k_x a - \cos k_y a)^2 \cos k_z d. \quad (\text{A3})$$

Note that the k_z summation in $\sum_{\mathbf{k}}$ is changed to $-\pi \leq k_z d \leq \pi$.

The LRC is also simplified for $c = 2d$:

$$\tilde{h}_1 = 0, \quad \tilde{h}_2 = \tilde{h}_4 = 4, \quad \tilde{h}_3 = -8 \quad (\text{A4})$$

$$V(\mathbf{q}) = \frac{V_c}{\det \tilde{V}} [\alpha(2 - \cos q_x a - \cos q_y a) + 4] \quad (\text{A5})$$

$$V'(\mathbf{q}) = \frac{V_c}{\det \tilde{V}} (4 \cos q_z d) \quad (\text{A6})$$

$$\det \tilde{V} = [\alpha(2 - \cos q_x a - \cos q_y a) + 4(1 - \cos q_z d)] \\ \times [\alpha(2 - \cos q_x a - \cos q_y a) + 4(1 + \cos q_z d)], \quad (\text{A7})$$

and $V_+(\mathbf{q}) = V'(\mathbf{q})$ and $V_-(\mathbf{q}) = 0$ in Eq. (51). Therefore Eq. (49) is reduced to

$$\kappa(\mathbf{q}, \omega) = \frac{(\kappa_{11}^0 + \kappa_{\cos}^0) [1 - (\kappa_{11}^0 - \kappa_{\cos}^0)(V(\mathbf{q}) - V'(\mathbf{q}))]}{[1 - (\kappa_{11}^0 + \kappa_{\cos}^0)(V(\mathbf{q}) + V'(\mathbf{q}))][1 - (\kappa_{11}^0 - \kappa_{\cos}^0)(V(\mathbf{q}) - V'(\mathbf{q}))]}, \quad (\text{A8})$$

$$= \frac{\kappa_{11}^0 + \kappa_{\cos}^0}{1 - (\kappa_{11}^0 + \kappa_{\cos}^0)(V(\mathbf{q}) + V'(\mathbf{q}))}. \quad (\text{A9})$$

The interaction is calculated as

$$V(\mathbf{q}) + V'(\mathbf{q}) = \frac{V_c/4}{\alpha(2 - \cos q_x a - \cos q_y a)/4 + 1 - \cos q_z d}. \quad (\text{A10})$$

On the other hand, one may start calculations by assuming $c = 2d$ in Fig. 1 and take a smaller unit cell. In this case, the systems is reduced to a single-layer model per unit cell. Following the previous work [61], one can easily obtain the LRC as

$$V_{\text{single}}(\mathbf{q}) = \frac{V_c^{\text{single}}}{\alpha_{\text{single}}(2 - \cos q_x a - \cos q_y a) + (1 - \cos q_z d)}, \quad (\text{A11})$$

where $V_c^{\text{single}} = \frac{e^2}{a^2(2d)} \frac{d^2}{2\epsilon_{\perp}}$ and $\alpha_{\text{single}} = \frac{\epsilon_{\parallel} d^2}{\epsilon_{\perp} a^2}$. We here recall that we have defined $V(\mathbf{q})$ and $V'(\mathbf{q})$ by dividing the unit cell volume $a^2 c$ in Eq. (27). Hence we also define V_c^{single} by dividing the same volume as $a^2(2d)$ to make a direct comparison between different formalisms possible.

The charge response function is then given by

$$\kappa_{\text{single}}(\mathbf{q}, \omega) = \frac{\kappa_{\text{single}}^0(\mathbf{q}, \omega)}{1 - V_{\text{single}}(\mathbf{q})\kappa_{\text{single}}^0(\mathbf{q}, \omega)}, \quad (\text{A12})$$

where

$$\kappa_{\text{single}}^0(\mathbf{q}, \omega) = \frac{2}{N} \sum_{\mathbf{k}} \frac{f(\xi_{\mathbf{k}}^{\text{single}}) - f(\xi_{\mathbf{k}+\mathbf{q}}^{\text{single}})}{\xi_{\mathbf{k}}^{\text{single}} + \omega - \xi_{\mathbf{k}+\mathbf{q}}^{\text{single}} + i\Gamma}, \quad (\text{A13})$$

and

$$\begin{aligned} \xi_{\mathbf{k}}^{\text{single}} = & -2t(\cos k_x a + \cos k_y a) - 4t' \cos k_x a \cos k_y a - 2t''(\cos 2k_x a + \cos 2k_y a) \\ & - 2t_z(\cos k_x a - \cos k_y a)^2 \cos k_z d - \mu \end{aligned} \quad (\text{A14})$$

Now we check that both approaches provide the same analytical results. The functional form of the dynamical charge susceptibility $\kappa(\mathbf{q}, \omega)$ in Eq. (A9) is the same as Eq. (A12). We can check from Eqs. (A2), (A3), (A13), and (A14)

$$\kappa_{11}^0 + \kappa_{\text{cos}}^0 = \kappa_{\text{single}}^0, \quad (\text{A15})$$

with the same band dispersion. The interaction parts Eqs. (A10) and (A11) are also identical because we can readily confirm $\alpha_{\text{single}} = \alpha/4$ and $V_c^{\text{single}} = V_c/4$.

We have proved analytically that $\kappa(\mathbf{q}, \omega)$ exhibits exactly 2π periodicity with respect to $q_z d$ when $c = 2d$ and $t_z = t'_z$, namely, 4π periodicity with respect to $q_z c$. It may be interesting to see how this periodicity changes as d is closer to $c/2$. Fixing $t_z = t'_z = 0.05$ and $\mathbf{q}_{\parallel} = (0.02\pi, 0)$, we compute $\text{Im}\kappa(\mathbf{q}, \omega)$ as a function of $q_z c$ for a sequence of d in Fig. 17.

In Fig. 17(a), both ω_{\pm} modes are clearly distinguished and we see approximately 2π periodicity. The intensity of the ω_{+} mode becomes very weak near $q_z c = 6\pi$ and 8π and apparently loses 2π periodicity. Nonetheless, we do not see a tendency that $\text{Im}\kappa(\mathbf{q}, \omega)$ would exhibit 4π periodicity. In Fig. 17(b), the difference between the ω_{\pm} modes is less visible as d is closer to $0.5c$, especially away from $q_z c = 2n\pi$. This is simply because we expect only one mode at $d = 0.5c$, i.e., in a single-layer case. The intensity of the ω_{+} mode at $q_z c = 2\pi$ and 8π is strongly suppressed. Yet we do not see a tendency toward 4π periodicity. At $d = 0.46c$ shown in Fig. 17(c), we eventually start to find a tendency that $\text{Im}\kappa(\mathbf{q}, \omega)$ could exhibit 4π periodicity and we finally obtain a perfect 4π periodicity at $d = 0.5c$ in Fig. 17(d).

In the right panels in Fig. 17 we plot the modulus of the denominator of $\kappa(\mathbf{q}, \omega)$ [see Eqs. (48) and (50)]. While the minimum value becomes relatively large around $q_z c = 2n\pi$ at

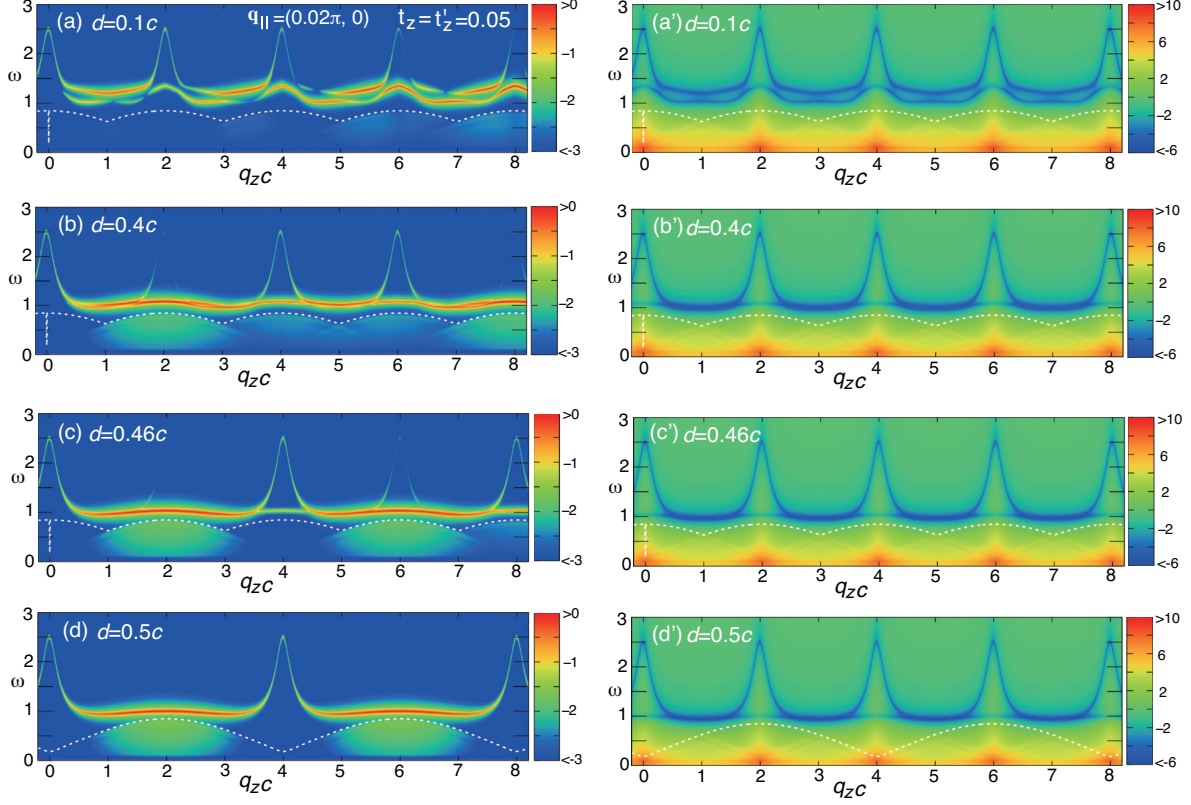


FIG. 17. Intensity map of $\log_{10} |\text{Im}\kappa(\mathbf{q}, \omega)|$ (left panels) and $\log_{10} |\partial \epsilon \epsilon|^2$ given in Eq. (50) (right panels) for various choices of intrabilayer distance d : (a) and (a') $d = 0.1c$, (b) and (b') $d = 0.4c$, (c) and (c') $d = 0.46c$, and (d) and (d') $d = 0.5c$. To get a reasonable contrast, the same color is used above 0 (10) and below -3 (-6) on the left (right) panels. The white dotted curve is the upper boundary of the continuum spectrum. The ω_- mode vanishes at $q_z c = 0$ for $d \neq 0.5c$ and this special feature is reflected as a spike of the dotted curve there.

$\omega \approx 1$ in Figs. 17(b')(c'), it is due to a relatively large mixture of the continuum spectrum broadened by a finite Γ [Eq. (36)]. We can check analytically that the denominator of $\kappa(\mathbf{q}, \omega)$ [Eqs. (48) and (49)] has 2π periodicity with respect to $q_z c$, including the case of $d = 0.5c$ as shown in Fig. 17(d'). A comparison with Figs. 17(a)–(d) demonstrates that the numerator of $\kappa(\mathbf{q}, \omega)$ determines the intensity of $\text{Im}\kappa(\mathbf{q}, \omega)$ and eventually leads to the 4π periodicity at $d = 0.5c$.

Appendix B: Split of ω_{\pm} modes at $q_z c = \pi$ for a small t_z

This appendix is supplementary to the discussion in the context of Fig. 5(c) and Fig. 6(b), where both ω_{\pm} modes seem nearly degenerate. However, there is a split between them, which may be less clear in the main text because we have taken a broadening parameter $\Gamma = 0.01$. The split of the ω_{\pm} modes is more visible when we take a smaller $\Gamma = 0.001$ as shown in Fig. 18(a). This split comes from the difference of the effective interaction $V(\mathbf{q}) \pm V_+(\mathbf{q})$ as explained in Eq. (62), not from a small value of t_z . In fact, the same split is present also for $t_z = 0$ as shown in Fig. 18(b). In this case the ω_+ mode also becomes gapless at $\mathbf{q}_{\parallel} = (0, 0)$.

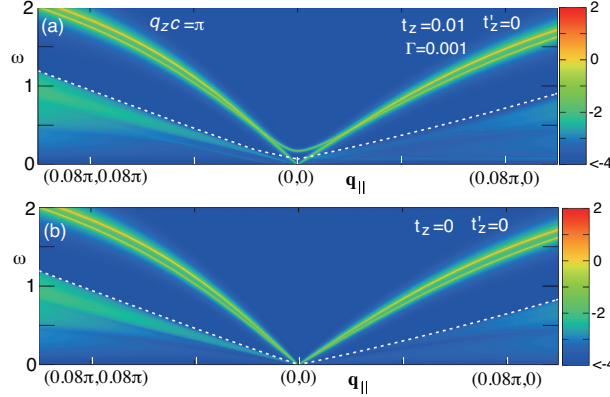


FIG. 18. Intensity map of $\log_{10} |\text{Im}\kappa(\mathbf{q}, \omega)|$ in the directions of $(0.1\pi, 0.1\pi) \rightarrow (0, 0) \rightarrow (0.1\pi, 0)$ for $q_z c = \pi$ at $t_z = 0.01$ (a) and 0 (b); the broadening parameter is taken as a smaller value $\Gamma = 0.001$. The split of the ω_{\pm} modes is clearly visible. This figure should be compared with Fig. 5(c). The white dotted curve is the upper boundary of the continuum spectrum. To keep an appropriate contrast, the same color is used below -4.

-
- [1] B. Keimer, S. A. Kivelson, M. R. Norman, S. Uchida, and J. Zaanen, “From quantum matter to high-temperature superconductivity in copper oxides,” *Nature* **518**, 179–186 (2015).
 - [2] P. W. Anderson, “The resonating valence bond state in La_2CuO_4 and superconductivity,” *Science* **235**, 1196–1198 (1987).
 - [3] D. J. Scalapino, “A common thread: The pairing interaction for unconventional superconductors,” *Rev. Mod. Phys.* **84**, 1383–1417 (2012).

- [4] T. R. Thurston, R. J. Birgeneau, M. A. Kastner, N. W. Preyer, G. Shirane, Y. Fujii, K. Yamada, Y. Endoh, K. Kakurai, M. Matsuda, Y. Hidaka, and T. Murakami, “Neutron scattering study of the magnetic excitations in metallic and superconducting $\text{La}_{2-x}\text{Sr}_x\text{CuO}_{4-y}$,” *Phys. Rev. B* **40**, 4585–4595 (1989).
- [5] J. Rossat-Mignod, L.P. Regnault, C. Vettier, P. Bourges, P. Burlet, J. Bossy, J.Y. Henry, and G. Lapertot, “Neutron scattering study of the $\text{YBa}_2\text{Cu}_3\text{O}_{6+x}$ system,” *Physica C: Superconductivity* **185-189**, 86–92 (1991).
- [6] J. M. Tranquada, B. J. Sternlieb, J. D. Axe, Y. Nakamura, and S. Uchida, “Evidence for stripe correlations of spins and holes in copper oxide superconductors,” *Nature* **375**, 561–563 (1995).
- [7] John M. Tranquada, Mark P. M. Dean, and Qiang Li, “Superconductivity from charge order in cuprates,” *Journal of the Physical Society of Japan* **90**, 111002 (2021).
- [8] G. Ghiringhelli, M. Le Tacon, M. Minola, S. Blanco-Canosa, C. Mazzoli, N. B. Brookes, G. M. De Luca, A. Frano, D. G. Hawthorn, F. He, T. Loew, M. Moretti Sala, D. C. Peets, M. Salluzzo, E. Schierle, R. Sutarto, G. A. Sawatzky, E. Weschke, B. Keimer, and L. Braicovich, “Long-Range Incommensurate Charge Fluctuations in $(\text{Y,Nd})\text{Ba}_2\text{Cu}_3\text{O}_{6+x}$,” *Science* **337**, 821–825 (2012).
- [9] M. Hashimoto, G. Ghiringhelli, W.-S. Lee, G. Dellea, A. Amorese, C. Mazzoli, K. Kummer, N. B. Brookes, B. Moritz, Y. Yoshida, H. Eisaki, Z. Hussain, T. P. Devereaux, Z.-X. Shen, and L. Braicovich, “Direct observation of bulk charge modulations in optimally doped $\text{Bi}_{1.5}\text{Pb}_{0.6}\text{Sr}_{1.54}\text{CaCu}_2\text{O}_{8+\delta}$,” *Phys. Rev. B* **89**, 220511 (2014).
- [10] Y. Y. Peng, M. Salluzzo, X. Sun, A. Ponti, D. Betto, A. M. Ferretti, F. Fumagalli, K. Kummer, M. Le Tacon, X. J. Zhou, N. B. Brookes, L. Braicovich, and G. Ghiringhelli, “Direct observation of charge order in underdoped and optimally doped $\text{Bi}_2(\text{Sr,La})_2\text{CuO}_{6+\delta}$ by resonant inelastic x-ray scattering,” *Phys. Rev. B* **94**, 184511 (2016).
- [11] L. Chaix, G. Ghiringhelli, Y. Y. Peng, M. Hashimoto, B. Moritz, K. Kummer, N. B. Brookes, Y. He, S. Chen, S. Ishida, Y. Yoshida, H. Eisaki, M. Salluzzo, L. Braicovich, Z. X. Shen, T. P. Devereaux, and W. S. Lee, “Dispersive charge density wave excitations in $\text{Bi}_2\text{Sr}_2\text{CaCu}_2\text{O}_{8+\delta}$,” *Nat. Phys.* **13**, 952 (2017).
- [12] R. Arpaia, S. Caprara, R. Fumagalli, G. De Vecchi, Y. Y. Peng, E. Andersson, D. Betto, G. M. De Luca, N. B. Brookes, F. Lombardi, M. Salluzzo, L. Braicovich, C. Di Castro,

- M. Grilli, and G. Ghiringhelli, “Dynamical charge density fluctuations pervading the phase diagram of a Cu-based high- T_c superconductor,” *Science* **365**, 906–910 (2019).
- [13] B. Yu, W. Tabis, I. Bialo, F. Yakhou, N. B. Brookes, Z. Anderson, Y. Tang, G. Yu, and M. Greven, “Unusual dynamic charge correlations in simple-tetragonal $\text{HgBa}_2\text{CuO}_{4+\delta}$,” *Phys. Rev. X* **10**, 021059 (2020).
- [14] W. S. Lee, Ke-Jin Zhou, M. Hepting, J. Li, A. Nag, A. C. Walters, M. Garcia-Fernandez, H. C. Robarts, M. Hashimoto, H. Lu, B. Nosarzewski, D. Song, H. Eisaki, Z. X. Shen, B. Moritz, J. Zaanen, and T. P. Devereaux, “Spectroscopic fingerprint of charge order melting driven by quantum fluctuations in a cuprate,” *Nat. Phys.* **17**, 53–57 (2021).
- [15] Haiyu Lu, Makoto Hashimoto, Su-Di Chen, Shigeyuki Ishida, Dongjoon Song, Hiroshi Eisaki, Abhishek Nag, Mirian Garcia-Fernandez, Riccardo Arpaia, Giacomo Ghiringhelli, Lucio Braicovich, Jan Zaanen, Brian Moritz, Kurt Kummer, Nicholas B. Brookes, Ke-Jin Zhou, Zhi-Xun Shen, Thomas P. Devereaux, and Wei-Sheng Lee, “Identification of a characteristic doping for charge order phenomena in Bi-2212 cuprates via RIXS,” *Phys. Rev. B* **106**, 155109 (2022).
- [16] Riccardo Arpaia, Leonardo Martinelli, Marco Moretti Sala, Sergio Caprara, Abhishek Nag, Nicholas B. Brookes, Pietro Camisa, Qizhi Li, Qiang Gao, Xingjiang Zhou, Mirian Garcia-Fernandez, Ke-Jin Zhou, Enrico Schierle, Thilo Bauch, Ying Ying Peng, Carlo Di Castro, Marco Grilli, Floriana Lombardi, Lucio Braicovich, and Giacomo Ghiringhelli, “Signature of quantum criticality in cuprates by charge density fluctuations,” *Nat. Commun.* **14**, 7198 (2023).
- [17] Eduardo H. da Silva Neto, Riccardo Comin, Feizhou He, Ronny Sutarto, Yeping Jiang, Richard L. Greene, George A. Sawatzky, and Andrea Damascelli, “Charge ordering in the electron-doped superconductor $\text{Nd}_{2-x}\text{Ce}_x\text{CuO}_4$,” *Science* **347**, 282–285 (2015).
- [18] Eduardo H. da Silva Neto, Biqiong Yu, Matteo Minola, Ronny Sutarto, Enrico Schierle, Fabio Boschini, Marta Zonno, Martin Bluschke, Joshua Higgins, Yangmu Li, Guichuan Yu, Eugen Weschke, Feizhou He, Mathieu Le Tacon, Richard L. Greene, Martin Greven, George A. Sawatzky, Bernhard Keimer, and Andrea Damascelli, “Doping-dependent charge order correlations in electron-doped cuprates,” *Science Advances* **2**, e1600782 (2016).
- [19] E. H. da Silva Neto, M. Minola, B. Yu, W. Tabis, M. Bluschke, D. Unruh, H. Suzuki, Y. Li, G. Yu, D. Betto, K. Kummer, F. Yakhou, N. B. Brookes, M. Le Tacon, M. Greven, B. Keimer,

- and A. Damascelli, “Coupling between dynamic magnetic and charge-order correlations in the cuprate superconductor $\text{Nd}_{2-x}\text{Ce}_x\text{CuO}_4$,” *Phys. Rev. B* **98**, 161114 (2018).
- [20] Hiroyuki Yamase, Matías Bejas, and Andrés Greco, “d-wave bond-order charge excitations in electron-doped cuprates,” *Europhys. Lett.* **111**, 57005 (2015).
 - [21] Zi-Xiang Li, Fa Wang, Hong Yao, and Dung-Hai Lee, “Nature of the effective interaction in electron-doped cuprate superconductors: A sign-problem-free quantum monte carlo study,” *Phys. Rev. B* **95**, 214505 (2017).
 - [22] Hiroyuki Yamase, Matías Bejas, and Andrés Greco, “Doping dependence of *d*-wave bond-charge excitations in electron-doped cuprates,” *Phys. Rev. B* **99**, 014513 (2019).
 - [23] Hiroyuki Yamase and Hiroshi Kohno, “Possible Quasi-One-Dimensional Fermi Surface in $\text{La}_{2-x}\text{Sr}_x\text{CuO}_4$,” *J. Phys. Soc. Jpn.* **69**, 332 (2000).
 - [24] Hiroyuki Yamase and Hiroshi Kohno, “Instability toward Formation of Quasi-One-Dimensional Fermi Surface in Two-Dimensional t-J Model,” *J. Phys. Soc. Jpn.* **69**, 2151 (2000).
 - [25] Christoph J. Halboth and Walter Metzner, “*d*-wave superconductivity and pomeranchuk instability in the two-dimensional Hubbard model,” *Phys. Rev. Lett.* **85**, 5162–5165 (2000).
 - [26] Matías Bejas, Andrés Greco, and Hiroyuki Yamase, “Possible charge instabilities in two-dimensional doped Mott insulators,” *Phys. Rev. B* **86**, 224509 (2012).
 - [27] Andrea Allais, Johannes Bauer, and Subir Sachdev, “Density wave instabilities in a correlated two-dimensional metal,” *Phys. Rev. B* **90**, 155114 (2014).
 - [28] H. Meier, C. Pépin, M. Einenkel, and K. B. Efetov, “Cascade of phase transitions in the vicinity of a quantum critical point,” *Phys. Rev. B* **89**, 195115 (2014).
 - [29] Yuxuan Wang and Andrey Chubukov, “Charge-density-wave order with momentum $(2q, 0)$ and $(0, 2q)$ within the spin-fermion model: Continuous and discrete symmetry breaking, preemptive composite order, and relation to pseudogap in hole-doped cuprates,” *Phys. Rev. B* **90**, 035149 (2014).
 - [30] W A Atkinson, A P Kampf, and S Bulut, “Charge order in the pseudogap phase of cuprate superconductors,” *New J. Phys.* **17**, 013025 (2015).
 - [31] Youichi Yamakawa and Hiroshi Kontani, “Spin-fluctuation-driven nematic charge-density wave in cuprate superconductors: Impact of Aslamazov-Larkin vertex corrections,” *Phys. Rev. Lett.* **114**, 257001 (2015).

- [32] Vivek Mishra and M. R. Norman, “Strong coupling critique of spin fluctuation driven charge order in underdoped cuprates,” *Phys. Rev. B* **92**, 060507(R) (2015).
- [33] Roland Zeyher and Andrés Greco, “Competition between spin-induced charge instabilities in underdoped cuprates,” *Phys. Rev. B* **98**, 224504 (2018).
- [34] K. Ishii, M. Fujita, T. Sasaki, M. Minola, G. Dellea, C. Mazzoli, K. Kummer, G. Ghiringhelli, L. Braicovich, T. Tohyama, K. Tsutsumi, K. Sato, R. Kajimoto, K. Ikeuchi, K. Yamada, M. Yoshida, M. Kurooka, and J. Mizuki, “High-energy spin and charge excitations in electron-doped copper oxide superconductors,” *Nat. Commun.* **5**, 3714 (2014).
- [35] W. S. Lee, J. J. Lee, E. A. Nowadnick, S. Gerber, W. Tabis, S. W. Huang, V. N. Strocov, E. M. Motoyama, G. Yu, B. Moritz, H. Y. Huang, R. P. Wang, Y. B. Huang, W. B. Wu, C. T. Chen, D. J. Huang, M. Greven, T. Schmitt, Z. X. Shen, and T. P. Devereaux, “Asymmetry of collective excitations in electron- and hole-doped cuprate superconductors,” *Nat. Phys.* **10**, 883–889 (2014).
- [36] Andrés Greco, Hiroyuki Yamase, and Matías Bejas, “Plasmon excitations in layered high- T_c cuprates,” *Phys. Rev. B* **94**, 075139 (2016).
- [37] Kenji Ishii, Takami Tohyama, Shun Asano, Kentaro Sato, Masaki Fujita, Shuichi Wakimoto, Kenji Tustsui, Shigetoshi Sota, Jun Miyawaki, Hideharu Niwa, Yoshihisa Harada, Jonathan Pelliciari, Yaobo Huang, Thorsten Schmitt, Yoshiya Yamamoto, and Jun’ichiro Mizuki, “Observation of momentum-dependent charge excitations in hole-doped cuprates using resonant inelastic x-ray scattering at the oxygen K edge,” *Phys. Rev. B* **96**, 115148 (2017).
- [38] G. Dellea, M. Minola, A. Galdi, D. Di Castro, C. Aruta, N. B. Brookes, C. J. Jia, C. Mazzoli, M. Moretti Sala, B. Moritz, P. Orgiani, D. G. Schlom, A. Tebano, G. Balestrino, L. Braicovich, T. P. Devereaux, L. Maritato, and G. Ghiringhelli, “Spin and charge excitations in artificial hole- and electron-doped infinite layer cuprate superconductors,” *Phys. Rev. B* **96**, 115117 (2017).
- [39] M. Hepting, L. Chaix, E. W. Huang, R. Fumagalli, Y. Y. Peng, B. Moritz, K. Kummer, N. B. Brookes, W. C. Lee, M. Hashimoto, T. Sarkar, J.-F. He, C. R. Rotundu, Y. S. Lee, R. L. Greene, L. Braicovich, G. Ghiringhelli, Z. X. Shen, T. P. Devereaux, and W. S. Lee, “Three-dimensional collective charge excitations in electron-doped copper oxide superconductors,” *Nature* **563**, 374–378 (2018).

- [40] Andrés Greco, Hiroyuki Yamase, and Matías Bejas, “Origin of high-energy charge excitations observed by resonant inelastic x-ray scattering in cuprate superconductors,” *Commun. Phys.* **2**, 3 (2019).
- [41] Andrés Greco, Hiroyuki Yamase, and Matías Bejas, “Close inspection of plasmon excitations in cuprate superconductors,” *Phys. Rev. B* **102**, 024509 (2020).
- [42] Jiaqi Lin, Jie Yuan, Kui Jin, Zhiping Yin, Gang Li, Ke-Jin Zhou, Xingye Lu, Marcus Dantz, Thorsten Schmitt, Hong Ding, Haizhong Guo, Mark P. M. Dean, and Xuerong Liu, “Doping evolution of the charge excitations and electron correlations in electron-doped superconducting $\text{La}_{2-x}\text{Ce}_x\text{CuO}_4$,” *npj Quantum Materials* **5**, 4 (2020).
- [43] Abhishek Nag, M. Zhu, Matías Bejas, J. Li, H. C. Robarts, Hiroyuki Yamase, A. N. Petsch, D. Song, H. Eisaki, A. C. Walters, M. García-Fernández, Andrés Greco, S. M. Hayden, and Ke-Jin Zhou, “Detection of Acoustic Plasmons in Hole-Doped Lanthanum and Bismuth Cuprate Superconductors Using Resonant Inelastic X-Ray Scattering,” *Phys. Rev. Lett.* **125**, 257002 (2020).
- [44] Maciej Fidrysiak and Józef Spałek, “Unified theory of spin and charge excitations in high-Tc cuprate superconductors: A quantitative comparison with experiment and interpretation,” *Phys. Rev. B* **104**, L020510 (2021).
- [45] M. Hepting, M. Bejas, A. Nag, H. Yamase, N. Coppola, D. Betto, C. Falter, M. Garcia-Fernandez, S. Agrestini, Ke-Jin Zhou, M. Minola, C. Sacco, L. Maritato, P. Orgiani, H. I. Wei, K. M. Shen, D. G. Schlom, A. Galdi, A. Greco, and B. Keimer, “Gapped collective charge excitations and interlayer hopping in cuprate superconductors,” *Phys. Rev. Lett.* **129**, 047001 (2022).
- [46] A. Singh, H. Y. Huang, Christopher Lane, J. H. Li, J. Okamoto, S. Komiya, Robert S. Markiewicz, Arun Bansil, T. K. Lee, A. Fujimori, C. T. Chen, and D. J. Huang, “Acoustic plasmons and conducting carriers in hole-doped cuprate superconductors,” *Phys. Rev. B* **105**, 235105 (2022).
- [47] M. Hepting, T. D. Boyko, V. Zimmermann, M. Bejas, Y. E. Suyolcu, P. Puphal, R. J. Green, L. Zinni, J. Kim, D. Casa, M. H. Upton, D. Wong, C. Schulz, M. Bartkowiak, K. Habicht, E. Pomjakushina, G. Cristiani, G. Logvenov, M. Minola, H. Yamase, A. Greco, and B. Keimer, “Evolution of plasmon excitations across the phase diagram of the cuprate superconductor $\text{La}_{2-x}\text{Sr}_x\text{CuO}_4$,” *Phys. Rev. B* **107**, 214516 (2023).

- [48] Abhishek Nag, Luciano Zinni, Jaewon Choi, J. Li, Sijia Tu, A. C. Walters, S. Agrestini, S. M. Hayden, Matías Bejas, Zefeng Lin, H. Yamase, Kui Jin, M. García-Fernández, J. Fink, Andrés Greco, and Ke-Jin Zhou, “Impact of electron correlations on two-particle charge response in electron- and hole-doped cuprates,” *Phys. Rev. Res.* **6**, 043184 (2024).
- [49] N. Nücker, H. Romberg, S. Nakai, B. Scheerer, J. Fink, Y. F. Yan, and Z. X. Zhao, “Plasmons and interband transitions in $\text{Bi}_2\text{Sr}_2\text{CaCu}_2\text{O}_8$,” *Phys. Rev. B* **39**, 12379–12382 (1989).
- [50] H. Romberg, N. Nücker, J. Fink, Th. Wolf, X. X. Xi, B. Koch, H. P. Geserich, M. Dürmler, W. Assmus, and B. Gegenheimer, “Dielectric function of $\text{YBa}_2\text{Cu}_3\text{O}_{7-\delta}$ between 50 meV and 50 eV,” *Zeitschrift für Physik B Condensed Matter* **78**, 367–380 (1990).
- [51] Ivan Bozovic, “Plasmons in cuprate superconductors,” *Phys. Rev. B* **42**, 1969–1984 (1990).
- [52] M. Bejas, V. Zimmermann, D. Betto, T. D. Boyko, R. J. Green, T. Loew, N. B. Brookes, G. Cristiani, G. Logvenov, M. Minola, B. Keimer, H. Yamase, A. Greco, and M. Hepting, “Plasmon dispersion in bilayer cuprate superconductors,” *Phys. Rev. B* **109**, 144516 (2024).
- [53] Alexander L Fetter, “Electrodynamics of a layered electron gas. II. periodic array,” *Annals of Physics* **88**, 1–25 (1974).
- [54] A. Griffin and A. J. Pindor, “Plasmon dispersion relations and the induced electron interaction in oxide superconductors: Numerical results,” *Phys. Rev. B* **39**, 11503–11514 (1989).
- [55] J.K. Jain and S. Das Sarma, “Elementary collective excitations in multilayered two-dimensional systems,” *Surface Science* **196**, 466–475 (1988).
- [56] J. Levallois, M.K. Tran, D. Pouliot, C.N. Presura, L.H. Greene, J.N. Eckstein, J. Uccelli, E. Giannini, G.D. Gu, A.J. Leggett, and D. van der Marel, “Temperature-dependent ellipsometry measurements of partial coulomb energy in superconducting cuprates,” *Physical Review X* **6**, 031027 (2016).
- [57] C. Boyd, L. Yeo, and P.W. Phillips, “Probing the bulk plasmon continuum of layered materials through electron energy loss spectroscopy in a reflection geometry,” *Physical Review B* **106**, 155152 (2022).
- [58] V. Z. Kresin and H. Morawitz, “Layer plasmons and high- T_c superconductivity,” *Phys. Rev. B* **37**, 7854–7857 (1988).
- [59] A. Bill, H. Morawitz, and V. Z. Kresin, “Electronic collective modes and superconductivity in layered conductors,” *Phys. Rev. B* **68**, 144519 (2003).

- [60] D. Grecu, “Plasma frequency of the electron gas in layered structures,” *Phys. Rev. B* **8**, 1958–1961 (1973).
- [61] F. Becca, M. Tarquini, M. Grilli, and C. Di Castro, “Charge-density waves and superconductivity as an alternative to phase separation in the infinite- U Hubbard-Holstein model,” *Phys. Rev. B* **54**, 12443–12457 (1996).
- [62] Feng-Lin Shyu and Ming-Fa Lin, “Plasmons and optical properties of semimetal graphite,” *Journal of the Physical Society of Japan* **69**, 3781–3784 (2000).
- [63] Sean M. Anderson, Bernardo S. Mendoza, Giorgia Fugallo, and Francesco Sottile, “Plasmon dispersion in graphite: A comparison of current ab initio methods,” *Phys. Rev. B* **100**, 045205 (2019).
- [64] O.K. Andersen, A.I. Liechtenstein, O. Jepsen, and F. Paulsen, “LDA energy bands, low-energy hamiltonians, t' , t'' , $t_{\perp}(k)$, and J_{\perp} ,” *Journal of Physics and Chemistry of Solids* **56**, 1573–1591 (1995).
- [65] Luciano Zinni, Matías Bejas, Hiroyuki Yamase, and Andrés Greco, “Low-energy plasmon excitations in infinite-layer nickelates,” *Phys. Rev. B* **107**, 014503 (2023).
- [66] J. M. Ziman, *Principles of the theory of solids* (Cambridge University Press, Cambridge, UK, 1976).
- [67] Mark S. Hybertsen, E. B. Stechel, M. Schluter, and D. R. Jennison, “Renormalization from density-functional theory to strong-coupling models for electronic states in Cu-O materials,” *Phys. Rev. B* **41**, 11068–11072 (1990).
- [68] R. S. Markiewicz, S. Sahrakorpi, M. Lindroos, Hsin Lin, and A. Bansil, “One-band tight-binding model parametrization of the high- T_c cuprates including the effect of k_z dispersion,” *Phys. Rev. B* **72**, 054519 (2005).
- [69] Niccolò Sellati and Lara Benfatto, “Ghost josephson plasmon in bilayer superconductors,” (2024), arXiv:2412.14927 [cond-mat.supr-con].
- [70] S. Pailhès, Y. Sidis, P. Bourges, C. Ulrich, V. Hinkov, L. P. Regnault, A. Ivanov, B. Liang, C. T. Lin, C. Bernhard, and B. Keimer, “Two resonant magnetic modes in an overdoped high T_c superconductor,” *Phys. Rev. Lett.* **91**, 237002 (2003).
- [71] S. Pailhès, C. Ulrich, B. Fauqué, V. Hinkov, Y. Sidis, A. Ivanov, C. T. Lin, B. Keimer, and P. Bourges, “Doping dependence of bilayer resonant spin excitations in $(Y, Ca)Ba_2Cu_3O_{6+x}$,” *Phys. Rev. Lett.* **96**, 257001 (2006).

- [72] Matías Bejas, Hiroyuki Yamase, and Andrés Greco, “Dual structure in the charge excitation spectrum of electron-doped cuprates,” *Phys. Rev. B* **96**, 214513 (2017).
- [73] Muhammad Zafur and Hiroyuki Yamase, “Spin and bond-charge excitation spectra in correlated electron systems near an antiferromagnetic phase,” *Phys. Rev. B* **109**, 245127 (2024).